Early warning signals for emerging infectious diseases

Qinghua Zhao[1,2,4], Nuno Moniz[2], Egbert H. van Nes[3], Marten Scheffer[3], Alexis Korotasz[1], Carly Barbera[1], Jason R. Rohr[1,4*]

[1]Department of Biological Sciences, Environmental Change Initiative, Eck Institute of Global Health, University of Notre Dame, Notre Dame, USA.

[2]Lucy Family Institute for Data & Society, University of Notre Dame

[3]Department of Environmental Sciences, Wageningen University, Wageningen, The Netherlands.

[4]These authors contributed equally.

[*]E-mail: jasonrohr@gmail.com.

Abstract

Establishing early warning systems for infectious disease outbreaks could save millions of lives by enabling rapid response and containment. One promising approach draws on the concept of critical slowing down (CSD)—a phenomenon in which complex systems lose resilience before tipping points—detected using resilience indicators (RIs) derived from the statistical properties of time series. While disease outbreaks may exhibit such early warning signals of critical transitions, most prior applications of CSD theory to global health have been limited to single diseases or locations, without broad assessments of predictive accuracy or lead time—the interval between the detection of warning signals and the onset of an outbreak. To address these limitations, we integrate CSD theory with time-to-event analyses to evaluate the predictive performance of 17 RIs across 31 infectious diseases in 134 regions worldwide. We find that both RIs and time-to-event analyses provide ample time to implement control measures, reliably anticipating outbreaks with a mean lead time of 17–21 days. Lead time was greater for pathogens with longer incubation periods and in regions with higher Human Development Index. Additionally, temperature and precipitation exhibited unimodal effects on lead time predictions for vector-borne and viral diseases. These findings highlight the value of incorporating socio-environmental drivers into outbreak forecasting models and lay the foundation for a local-to-global early warning system capable of guiding proactive public health interventions.

Key words

Infectious diseases, Early Warning Signals, Lead time, Critical slowing down, Time-to-event analysis, Socio-ecological drivers

Introduction

Infectious diseases frequently re-emerge, driven by factors such as shifting human movement patterns, waning immunity, or reduced vaccine uptake (*1*). These resurgences cause millions of deaths worldwide each year; therefore, the ability to predict infectious disease outbreaks weeks in advance could save countless lives and significantly improve global quality of life (*2*). Several approaches can theoretically be used to anticipate outbreaks (*2–4*), such as applying dynamical mathematical models, monitoring Google searches and social media posts, wastewater surveillance for pathogens, and calculating generic, model-free statistical properties of time series as early warning signals (EWSs) of complex systems approaching critical transitions or "tipping points" (*5–7*). The value of using statistical properties of time series as EWSs is that they tend to require less effort and money than parameterizing dynamical models or monitoring wastewater for pathogens, and have regularly out-performed Google search and social media surveillance (*2*). Additionally, across many complex systems, statistical properties of time series are well linked to critical slowing down or reduced resilience (i.e., the ability to maintain normal stabilizing dynamics, e.g., a disease-free state, when subjected to disturbances) as systems approach critical transitions (*2*), which is why these types of EWSs are often referred to as resilience indicators (RIs). Measuring a system's slowed recovery from a perturbation can be challenging, so statistical properties of time series, such as changes to the variance or autocorrelation, are used as RIs or proxies of critical slowing as systems approach tipping points (*2*). Importantly, it is well documented that there were RIs in time series of past earthquakes, state shifts in ocean circulation systems and climate, and collapses of the global financial market, societies, and ecosystems (*5–7*). The application of RIs to human health has been more limited, but RIs have been detected for asthmatic attacks, mood depression, and epileptic seizures (*5–7*).

Recently, there has been interest in applying resilience theory to anticipate infectious disease outbreaks (*1*, *2*, *8–11*). Mathematically, the critical transition in models of infectious diseases is a piecewise continuous transcritical bifurcation, whereby self-limiting, stuttering chains of infection that inevitably go extinct shift to major outbreaks of sustained human-to-human transmission (*1*, *9*). When the reproduction number, R (the number of people in a population who can be infected by an individual at any specific time), is below the critical threshold of 1, the system is stabilized at a relatively disease-free state (i.e., few cases are observed), whereas above

1, the disease-free state becomes unstable and the introduction of a single infected individual can trigger an outbreak (*2*). Simple models of disease emergence show evidence of critical slowing down across a wide range of parameter values (*1*, *9*) and under varying conditions of ignorance and uncertainty (*12*, *13*), suggesting that RI-based EWSs for disease outbreaks might be common.

Recently, RIs were detected for malaria resurgence in Kenya (*10*) and COVID-19 waves (*14*), but the application of RIs to shifts from endemic disease-free to epidemic disease-emergence states have been predominantly theoretical and studies of real-world data have focused mostly on single diseases, regions, and RIs with inconsistent success (*1*, *2*, *8*, *11*–*13*). Hence, the use of RIs to offer reliable EWSs across infectious diseases remains equivocal. Additionally, little is known about the combinations of multiple RIs that could maximize EWS performance (Fig. 1), the performance of RIs across different types of diseases, or the traits of pathogens and locations that affect outbreak predictions and lead times (how early an outbreak is anticipated; Fig. 1), the latter of which is critical because it determines the amount of time communities have to prevent or mitigate an impending outbreak (but see (*9*)). Another major knowledge gap is that, unlike dynamical models or wastewater and social media monitoring, traditional RI-based approaches do not actually predict the probability or the timing of a critical transition because they never treat the timing of the actual transition (i.e., outbreak) as the dependent variable. Rather, RI-based approaches use a significant positive relationship between the RIs (dependent variable) and time before the critical transition (independent variable) as an indirect estimate of an impending state shift in the system, despite there being a well-established class of statistical analyses for studying how long it takes for a binary event to happen, which is referred to as time-to-event, failure time, or survival analyses (Fig 1).

To fill these gaps in understanding, we analyzed a high-resolution global dataset of daily incidence for 31 human infectious diseases across 134 regions worldwide (Fig 2), comprising 302 outbreaks (see Materials and Methods for a list of diseases). Among these 31 diseases, 64% were zoonotic, 58% were zoonotic diseases with a wildlife reservoir, 35% were vector-borne, and 54%, 35%, and 5% were caused by viruses, bacteria, and protozoa, respectively (Fig. 2). Using this dataset, we tested 17 RIs in total, 11 commonly used RIs, 4 RIs identified from machine learning and new modelling techniques, and 2 RIs specifically designed for time series influenced by seasonal forcing. To test for the significance of the RIs, we advanced a moving window forward

106 towards the outbreak, testing for a significant positive association between the RIs and
107 time in each window based on a Kendall τ rank correlation statistic (see Material and
108 Methods). The performance of the RI in predicting outbreaks was evaluated based on its
109 true positive and negative rates (i.e., using the area under the receiver operating
110 characteristic curve (AUC)) and 5-fold cross validation. For outbreaks that could be
111 predicted using an RI, we calculated the lead time as the days between the first
112 instance that τ was significant and the start of the outbreak (Fig. 1). In contrast to this
113 traditional RI approach, we also used a time-to-event, Cox proportional hazards
114 analysis to more directly predict lead time and test predictors of the timing of
115 outbreaks.
116
117 **Evaluating resilience indicators and lead times**
118 Across all 31 diseases, we found that the best performing single RI across moving
119 window lengths was Standard Deviation (mean AUC=0.93 from cross validation, window
120 length=10 days) (Fig 3a-b, S1). Importantly, the performance of Standard Deviation
121 extends beyond what can be explained simply by trends in the mean incidence. Indeed,
122 trends in the mean incidence exhibit lower maximum predictive power (AUC=0.70, Fig
123 S2) compared to those of Standard Deviation or the first-order autoregressive model
124 (AR-1; AUC=0.87, Fig S1h). While the Standard Deviation provides the highest overall
125 predictive performance, the observed increase in AR-1 prior to outbreaks is particularly
126 notable, as autocorrelation is widely regarded as a robust indicator of CSD (*15*).
127 Therefore, the concurrent rise in both Standard Deviation and AR-1 suggests that the
128 predictive power of our early warning approach is indeed rooted in the generic
129 phenomenon of CSD. Combining the Standard Deviation with other resilience indicators
130 (RIs) did not enhance predictive accuracy, as the mean AUC from cross-validation did
131 not improve when Standard Deviation was combined with either the top-performing RIs
132 or those least correlated with it, despite improvements observed in the raw (non-cross-
133 validated) AUC (Fig 3a, 3b). Hence, using the raw AUC rather than the mean AUC from
134 cross validation can result in overfitting and thus overly optimistic estimates of model
135 performance. For the best RI (Standard Deviation), the mean lead time was 17.7 days
136 (±1.3 s.e.; Fig. 4) across times series and diseases. The time-to-event analyses, which
137 captures both the likelihood of an outbreak and its timing, also produced a dependable
138 model, accounting for 65.6% (marginal R^2) of the variation in the hazard of an outbreak
139 (Fig. S3). The higher τ value from the best RI (Standard Deviation) was negatively

140 associated with the time to an outbreak in the time-to-event analyses (Fig. S3b) and
141 thus a higher hazard of an outbreak (Fig. S3a), reflecting the consistency between the
142 traditional RI and time-to-event models. The time-to-event analysis estimated a mean
143 lead time of 21.3 days (±1.2 s.e.; Fig. S4), which is 3.6 days longer than the estimate
144 provided by the traditional RI approach. Importantly, given that major outbreaks do not
145 happen immediately after $R_e = 1$ (*9*), the actual lead time likely exceeds these estimates.
146 Overall, these results suggest that both RI and time-to-event analyses reliably warn of
147 upcoming outbreaks, and the average warning provided by RIs of 17-21 days or greater
148 is enough time to mitigate, and possibly even prevent, outbreaks.
149 Given that many datasets provide weekly rather than daily case report data, we
150 reconducted our models averaging the daily data of each week. Notably, the coarser-
151 scale weekly data resulted in lower AUC values (Fig. S5) and a mean lead time of 50.6
152 days (Fig. S6), which is > 30 days longer than the lead time from the daily data. This
153 indicates that temporally coarse data resolution can provide an overly optimistic
154 estimation of lead times for outbreak mitigation and prevention. Therefore, the use of
155 finer-scale daily data is highly recommended for more reliable EWS assessments and
156 lead time estimates.
157
158 **How traits of pathogens and outbreak locations affect both lead time and outbreak**
159 **risk**
160 Next, using the daily data, we sought to identify the traits of pathogens and
161 outbreak locations that could explain variation in the time to outbreak occurrence and
162 lead times predicted by the best RI (Standard Deviation). We hypothesized that
163 outbreaks caused by pathogens with shorter incubation times (the interval between
164 exposure to a pathogen and the appearance of the first symptoms) would be harder to
165 anticipate and would have shorter lead times than those with longer incubation times.
166 Temperature and precipitation were expected to exhibit hump-shaped relationships
167 with time to outbreak occurrence and lead time, as these environmental factors are
168 known for unimodal effects on transmission dynamics and pathogenesis (*16*),
169 particularly for vector-borne pathogens, all of which have ectothermic hosts that are
170 often more sensitive to climatic factors than endothermic hosts. Additionally, given that
171 vector-borne pathogens tend to have greater frequency- than density-dependent
172 transmission (*17*), we postulated no relationship between lead time and human
173 population density for these pathogens. Finally, given that more developed areas have

174 greater outbreak surveillance, health infrastructure, and case reporting, we
175 hypothesized that regions with a higher Human Development Index (HDI; a statistical
176 composite of life expectancy, years of education, and per capita income) (*18*) would have
177 a longer lead times than regions with lower HDIs. Additionally, we predicted that HDI
178 would be negatively associated with the risk of disease outbreaks for vector-borne
179 diseases because they are often effectively combatted by costly insecticide applications
180 and homes with windows or screens (*19*, *20*). To test these *a priori* hypotheses, we
181 developed a baseline generalized linear mixed effects model for lead times predicted by
182 the best RI (Standard Deviation) and a Cox proportional hazards model for time to
183 outbreak occurrence, and removed nonsignificant factors through a backwards
184 selection process to reach a final model (see Materials and Methods, Table S1-S2).
185 These analyses revealed considerable variation in lead times and time to outbreak
186 occurrence across the time series and 31 diseases. For example, as predicted,
187 pathogens that spread rapidly because they have short incubation times also had short
188 lead times, with each natural log increase in days of incubation time increasing lead
189 time by 0.11 $\pm$0.05 day (mean$\pm$s.e) (Fig. 4c). Additionally, on average, vector-borne and
190 viral pathogens offered shorter lead times (12.5 and 16.1 days) than non-vector-borne
191 and bacterial pathogens (19.2 and 19.0), respectively (Fig. 4a, 4b). However, when
192 temperature and precipitation were near their mean values, lead times peaked for both
193 vector-borne and non-vector-borne pathogens, and vector-borne pathogens had shorter
194 lead times than non-vector-borne pathogens (Fig. 4a, 4b). In fact, at mean temperature
195 and precipitation, lead times were 40.0 and 27.0 days, respectively, for vector-borne
196 diseases, and approximately 50.0 and 50.0 days, respectively, for non-vector-borne
197 diseases (Fig. 4a, 4b). Additionally, vector-borne diseases occurred under more narrow
198 temperature conditions and peaked at warmer temperatures (20.4 °C vs 13.3 °C) than
199 non-vector-borne diseases (Fig. 4a), consistent with the well-documented sensitivity of
200 vector-borne pathogens to environmental conditions and greater frequency of vector-
201 borne diseases in warmer than cooler regions (*16*).
202 Whereas lead times for both vector- and non-vector-borne diseases responded
203 unimodally to temperature, only viral pathogens were unimodally associated with
204 temperature, peaking near observed mean temperatures (13.1 °C) (Fig 4d). In contrast,
205 bacterial pathogens were associated positively with temperature for both lead time and
206 time to outbreak occurrence (Fig. 4d, 5b). Consistent with these findings, several
207 studies documented hump-shaped relationships between arboviruses and temperature

208 (*16*), whereas bacterial biological rates (*21*) and infections in humans regularly show
209 positive associations with environmental temperature (*22*). Precipitation exhibited a
210 unimodal relationship with both lead time and time to outbreak occurrence for vector-
211 borne and non-vector-borne diseases (Fig. 4b, 5c) and a unimodal relationship with lead
212 time for viral pathogens (Fig. 4e), consistent with previous studies documenting
213 unimodal relationships between precipitation and these pathogen types (*23*, *24*). In
214 contrast, precipitation was negatively associated with lead time for bacterial infections
215 (Fig. 4e), aligning with previous research documenting that higher precipitation levels
216 facilitate more rapid transmission of bacterial pathogens (*22*, *25*).

217 As predicted, lead time was associated positively with HDI, presumably because
218 wealthier locations invest more in health infrastructure and pathogen surveillance that
219 can facilitate earlier detection of human cases of disease (Fig. 4f). This positive
220 association between lead time and HDI was significant across all diseases (Fig. 4f). The
221 time-to-event analysis further revealed an HDI-by-vector-borne-disease interaction, with
222 vector-borne diseases showing a positive association between HDI and time to outbreak
223 occurrence (Fig. 5d). In fact, a shift from the low to high HDI category more than halved
224 the hazard of a vector-borne disease outbreak (Fig. 5d). These results are consistent
225 with vector-borne diseases being reduced by human development more than non-
226 vector-borne diseases, thus lengthening the time to vector-borne disease outbreaks. For
227 example, many vector-borne diseases can be effectively managed by costly home
228 improvements and insecticide applications (*19*, *20*). Hence, development can enable
229 earlier detection and thus mitigation and prevention of environmentally mediated
230 diseases.

231 Time series length was associated positively with lead time (Fig. S7a) and time to
232 outbreak occurrence (Fig. S7b), suggesting that early initiation of monitoring and case
233 reporting (*26*, *27*), the availability of longer historical datasets (*28*), or an enhanced
234 commitment to outbreak surveillance (*29*) might enable stakeholders to extend lead
235 times before an outbreak. Additionally, neither outbreak type (first or subsequent in the
236 time series) nor human population density had significant effects on lead time or the
237 hazard of outbreak occurrence (Fig. S8 & S9). However, we admonish against assuming
238 that these factors do not affect these endpoints, as increased statistical power or a
239 different subset of human diseases could produce different results.

240 While our study provides critical advancements in the development and
241 application of resilience theory for predicting disease outbreaks, we acknowledge

242 potential misclassifications of case data stemming from reporting biases, diagnostic
243 inaccuracies, or surveillance inconsistencies, which may introduce uncertainties and
244 weaken the robustness of warning indicators. Importantly, these misclassifications
245 should only amplify random errors in our analyses that would reduce the likelihood of
246 detecting RIs that warn of impending outbreaks. Nevertheless, we discovered EWSs
247 despite this impediment. Another important limitation of our analyses is that they are
248 restricted to gradual endemic states of pathogen transmission rather than abrupt
249 emergence of outbreaks involving new strains (e.g., a reassortant influenza virus) or
250 pathogens (e.g., de novo spillover of a human-to-human transmissible pathogen from a
251 zoonotic reservoir) to a region (*11*). Expanding the framework to incorporate RIs for new
252 pathogens, such as those that spillover from wildlife to humans, and artificial
253 intelligence (*11*, *30*) would enhance its utility in broader public health contexts.
254

255 **Implications and Conclusions**

256 Our study provides a significant advancement in the development and application
257 of EWSs for infectious disease outbreaks. By systematically evaluating multiple RIs
258 across a diverse set of diseases and geographic locations, we identified key predictive
259 factors that enhance outbreak forecasting. Shifting to time-to-event analysis from the
260 traditional RI-based approach improved both the accuracy of outbreak predictions and
261 lengthened lead time, providing a more reliable framework for early intervention.

262 Importantly, we demonstrate that pathogen characteristics, climate, and socio-
263 economic factors significantly influence lead time and outbreak timing, highlighting the
264 need for context-specific forecasting models. Our findings show that pathogen
265 incubation time is associated positively with lead time. Additionally, higher HDI regions
266 experience longer lead times and reduced outbreak risks for vector-borne diseases,
267 suggesting that public health infrastructure and surveillance capacity play crucial roles
268 in disease prevention. Furthermore, we emphasize the need for high-resolution
269 temporal data, as coarse-scale weekly data may lead to overly optimistic lead time
270 estimates, potentially compromising timely responses.

271 This research lays the foundation for a global disease forecasting system that
272 integrates real-time data streams and model-free statistical techniques to enhance
273 predictive accuracy (*11*). Future work should focus on expanding the range of predictive
274 indicators and developing interactive platforms for real-time outbreak monitoring. By
275 improving our ability to anticipate and mitigate outbreaks, our study contributes to

strengthening public health preparedness and minimizing the societal and economic impacts of infectious diseases.

Figures

Figure 1. An overview of the data and methods used in this paper. **a.** The entire dataset of time series was divided into two groups, those with (i.e. the average number of secondary infections caused by a single infected individual at a given time point, $R_e \geq 1$; red line at **b**) and without outbreaks. **b**. Next, the most accurate resilience indicator (RI) was identified by considering single or combinations of RIs (see Methods section) with accuracy determined by taking the area under the receiver operating characteristic curve of 100 runs of a 5-fold cross validation. **b**. Once the most accurate RI was established, we quantified lead time or how early an outbreak could be anticipated (i.e., days between the start of an outbreak and the point that the RI first became significant). Next, we tested whether lead time was affected by the traits of the pathogens and geographic locations of the outbreak. Last, given that traditional RI analyses only indirectly predict outbreaks by testing correlations between RIs and time, time-to-event analyses were employed to more directly predict the timing of outbreaks and lead time.

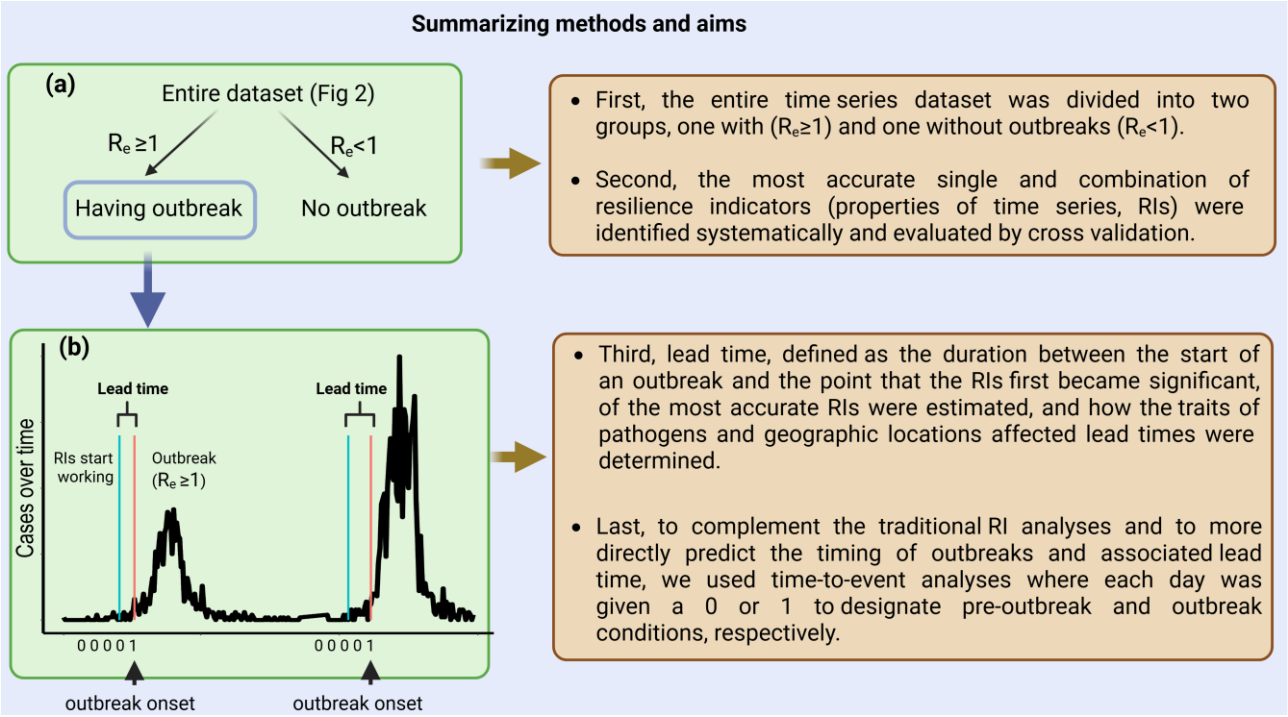

Figure 2. The studied locations (a), total number of diseases (b), and total number of time series (c) grouped by pathogen- and disease-type categories. See Table S4 for details of diseases, regions, and pathogen types.

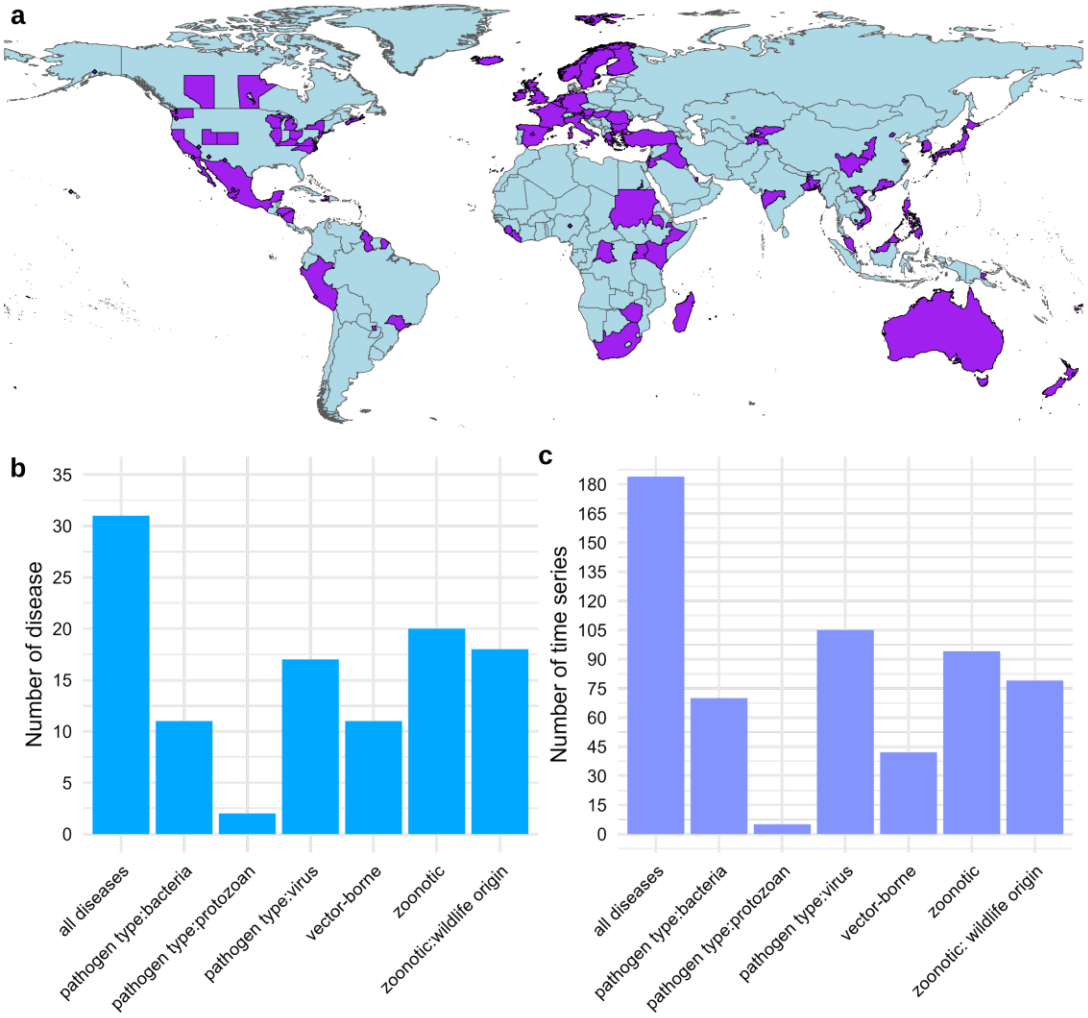

Figure 3. The accuracy of resilience indicators (RIs) as early warning signals (EWSs) of outbreaks across 31 diseases, examined using mean area under the receiver operating characteristic curves (AUC) and cross validation. All RIs used the window length (i.e. 10 days) that maximized the AUC for the most accurate RI (i.e. Standard Deviation; mean AUC=0.93 from cross-validation) (**a-b**) across all RIs and window lengths (Fig S1). We sequentially added either the next best performing single RI (**a**) or the next most orthogonal RI (i.e., least correlated based on Principal Component Analysis) to the best performing RI (**b**) until we tested up to four total RIs in our models. Importantly, sequentially adding the next most orthogonal RI to the model ensures that the baseline AUC goes up with each RI addition, but it does not guarantee that the mean AUC from the cross validation will continually rise with each added RI. Standard deviation: SD, index of dispersion: ID, first differenced variance: FD, skewness: SK, autocorrelation at lag 1: AR1, autocovariance: AU, autocorrelation at lag 2: AR2. The AUC values in parenthesis at **a-b** represent the mean and s.d from cross-validation.

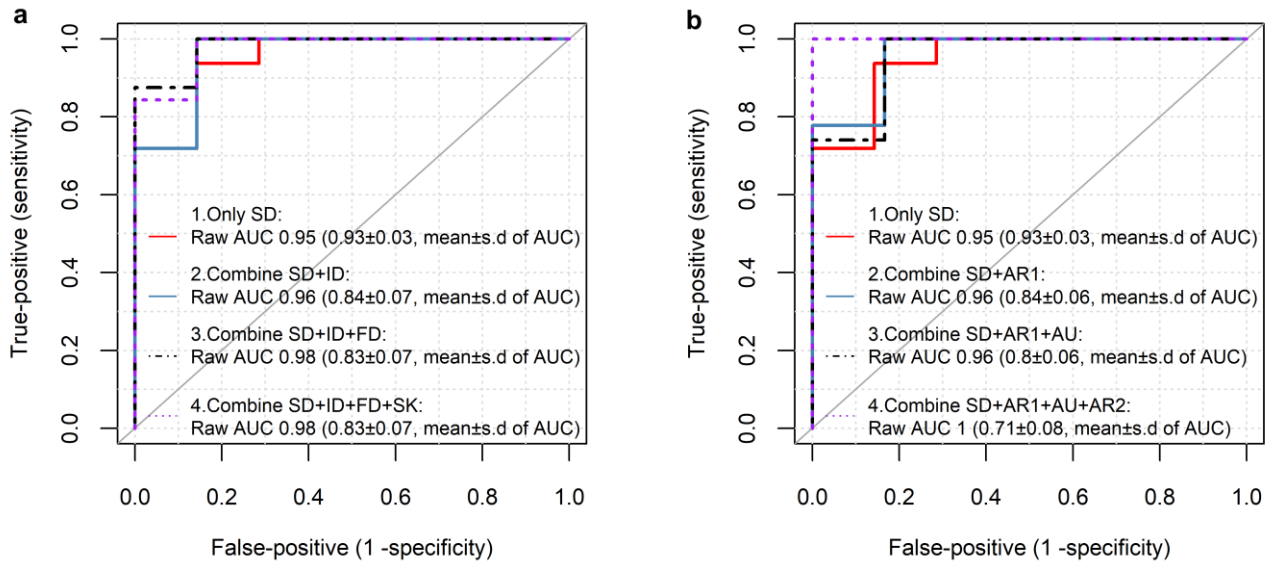

Figure 4. **A display of the main effects and interactions that were significantly associated with lead time.** The bold lines and gray bands depict best-fit lines and 95% confidence bands (or standard error in panel f), respectively, derived from the predicted values of the final statistical model that is available in Table S1. In panel **f**, the significance between groups was assessed using the emmeans function from the emmeans package. For the effects of time series length and population density on lead time, refer to Fig S7-S9. Statistical results see table S1. HDI represents the Human development index.

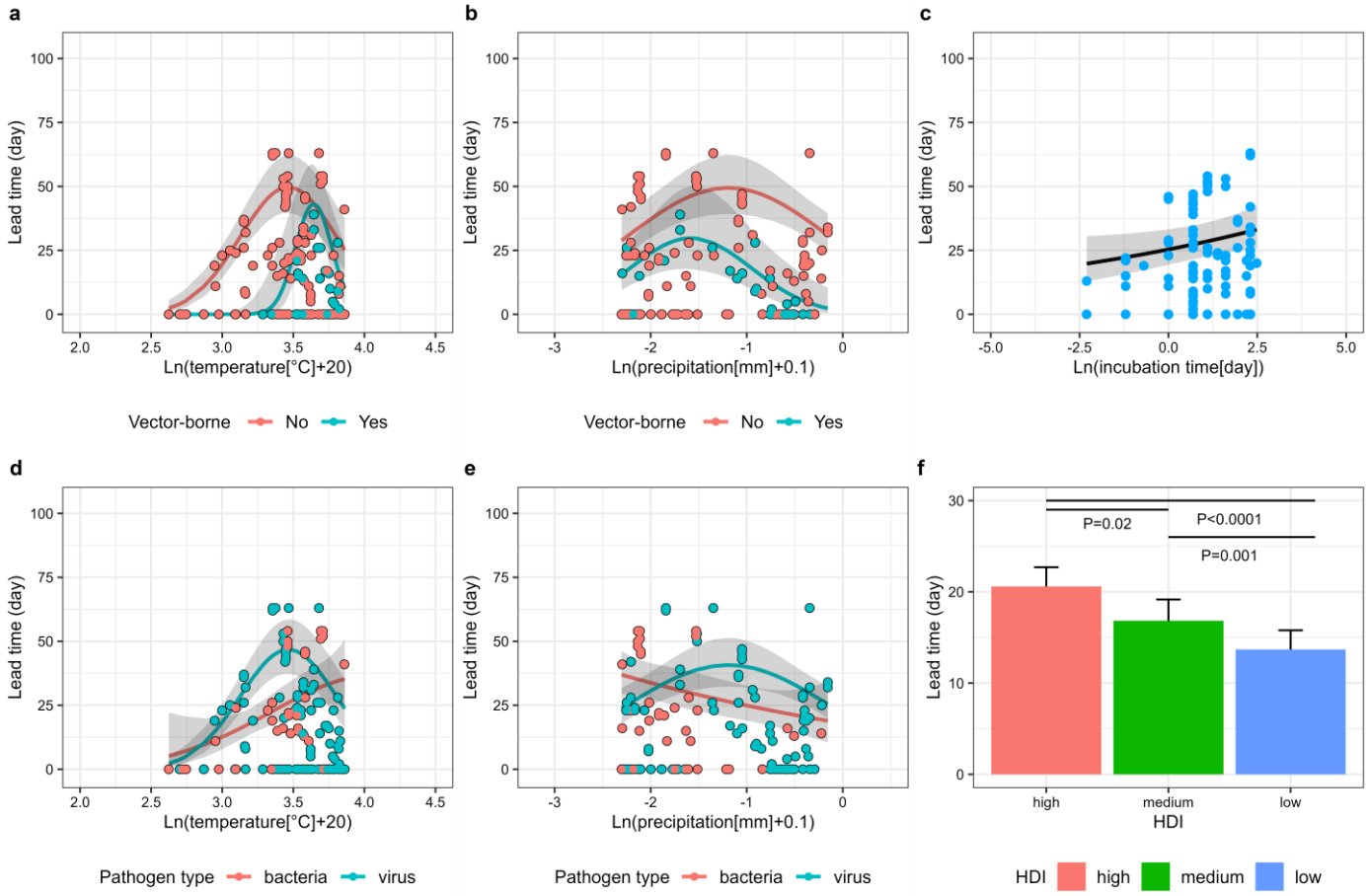

Figure 5. Coefficients ± s.e (a) and plots of significant predictors (b-d) from a Cox proportional hazards mixed model examining the effects of various factors on time to outbreak occurrence. **a**, A positive coefficient signifies an increased hazard of outbreak occurrence, and consequently a reduced time until an outbreak. A significant quadratic coefficient indicates a second-order polynomial function between a predictor and hazard of outbreak occurrence. The bold lines and gray bands depict best-fit lines and 95% confidence bands (or standard error in panel f), respectively, derived from the predicted values of the final statistical model that is available in Table S3. **d**, the significance between groups was assessed using the emmeans function from the emmeans package. Significant effects are indicated by *P <0.05, **P < 0.01, ***P < 0.001. HDI represents the Human development index.

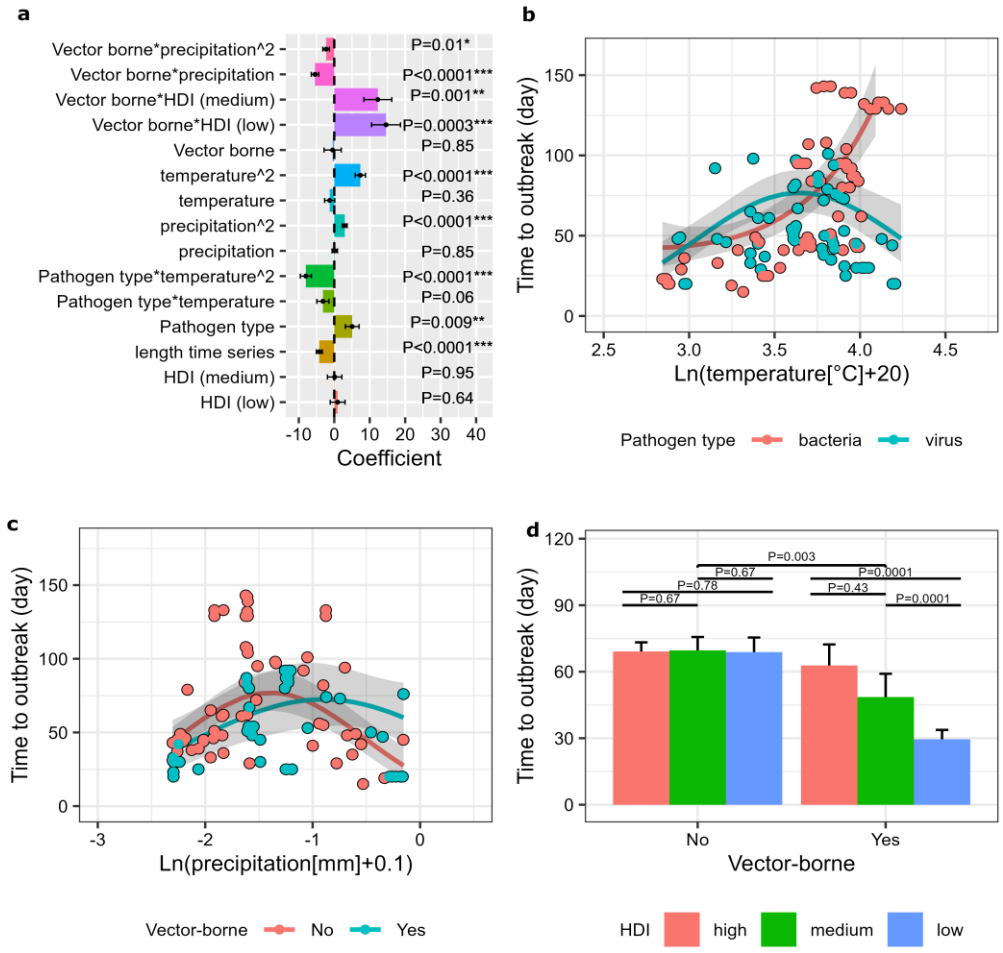

Methods

Disease dataset. For our analyses, we used the subset of the Analytics for Investigation of Disease Outbreaks (AIDO) dataset (https://aido.bsvgateway.org/) with daily reported disease case data and time series ≥1 week. This resulted in 31 diseases across 134 regions (i.e. either country or administrative level e.g. municipality and province; Fig 2), comprising 184 time series (Fig 2) with an arithmetic mean length of 117 days (±14 s.e.) (see Table S4 for the corresponding regions and time series length for each disease). The 31 diseases included in this dataset are Anthrax, Brucellosis, Campylobacteriosis, Chikungunya, Cholera, Dengue, Ebola, Gastroenteritis, Lassa Fever, Leptospirosis, Malaria, Marburg, Measles, Middle East Respiratory Syndrome, Monkeypox, Nipah, Norovirus, Novel Influenza A, Pertussis, Plague, Polio, Q Fever, Rift Valley Fever, Rubella, Salmonellosis, Shiga Toxin-Producing E. Coli, Shigellosis, Tularemia, West Nile Virus, Yellow Fever, Zika.

Socio-economic and eco-environmental factors. We gathered covariates, all of which were matched to each time series and corresponding location in the disease dataset. Daily temperature (°C) and precipitation (mm) were retrieved from NOAA's National Centers for Environmental Information (*31*). Annual human development index (HDI) for each 5 arc-minute gridded unit (latitude and longitude) was sourced from Kummu et al. (*18*). and subsequently aggregated to the respective country or administrative level using arithmetic means. Yearly population density (people per km^2) was retrieved from the Center for International Earth Science Information Network database (*32*). Across all studied locations, the yearly resolution was used for HDI and population density because this was the only temporal resolution available. For each pathogen at a given location, the incubation time (day) was retrieved from the literature. Population density and incubation time were natural log transformed to ensure normality. Precipitation data were transformed using $\ln(x + 0.1)$ to accommodate zero values, while temperature data were transformed using $\ln(x + 20)$ to adjust for temperatures below -10°C in certain regions (e.g. Nordic countries such as Finland).

Traditional RI analyses. Using the methods of Cori et al. (*33*) (because it outperforms others approaches (*34*); for details of these methods, see Supplementary Information 1), we first delineated the start of each outbreak in each time series as the point when R_e (i.e. the average number of secondary infections caused by a single infected individual at a given time point) (*11*, *33*, *34*) was ≥1. Thus, each time series was divided into no outbreak and outbreak sections (all code archived on GitHub (*35*)). Of the 184 time

series, 27 did not have any days where R_e was ≥1, representing no outbreak time series. Of the remaining 157 time series, 68 (43.3%) had a single outbreak, and 89 (56.7%) had multiple outbreaks, resulting in 302 outbreaks in total (see Fig S10 for the frequency of outbreaks). For each time series, we then utilized 11 commonly used RIs (standard deviation, skewness, kurtosis, coefficient of variation, first differenced variance, autocovariance, index of dispersion, density ratio, autocorrelation at lag 1, lag 2 and lag 3), 2 RIs specifically designed for time series influenced by seasonal forcing (wavelet filtering, wavelet reddening), and 4 RIs developed by machine learning, empirical dynamic modeling, or previously untested in the context of infectious diseases (relative dispersion, time series acceleration, the absolute value of dominant eigenvalue, and hurst exponent), resulting in a total of 17 RIs (*35*) (Table S5 and Supplementary Information 2).

Following Dakos et al. (*36*), we adopted a moving window approach to test for a positive association between each RI and time as it approached $R_e \geq 1$. Before conducting the moving window approach, each disease time series was detrended using Gaussian smoothing (*36*). The length of the moving window varied from 7 to 21 days (1 to 3 weeks) with increments of 1 day (Fig S1). The magnitude of the association between each RI and time in each window was measured using the nonparametric Kendall τ rank correlation statistic (*36*). The significance of the τ was determined by estimating the fraction of 100 null surrogates that performed better than the observed dataset using the method of Ebisuzaki (*37*). These randomized surrogate datasets have the same power spectra and autocorrelation structure of the original data but with randomized phases to eliminate spurious results because of the correlation in time.

Next, we employed receiver operating characteristic (ROC) curves to quantify the performance of each RI using 100 runs of 5-fold cross validation (i.e., 80% training data and 20% testing data), performed with the caret package (*38*). The cross-validation aimed to test out-of-sample model performance to determine if our models were underfit, overfit, or "well-generalized". Cross-validation was performed to evaluate the predictive performance of RIs, rather than assess the fit to the raw case time series itself. For each of 100 runs, the area under the ROC curve (AUC) was computed to quantify the model's discrimination ability, with a larger AUC indicating higher true positive and negative rates and thus higher accuracy. The arithmetic mean AUC obtained from 100 runs of cross-validation was taken as the final performance metric to assess the accuracy performance of each RI. Given that the length of the moving

window can impact the AUC of an RI, the optimal moving window length was chosen for each RI by selecting the window length between 7 and 21 days with the highest mean AUC in the cross validations (Fig S1).

Once the most accurate single RI was determined, we tested whether combining up to four RIs would improve model predictions based on AUC and cross validation. Specifically, we forced all RIs to use the window length that maximized the AUC for the most accurate RI (i.e., Standard deviation with window length=10 days in Fig S1). Next, we conducted Principal Component Analyses (PCA) to determine associations among the RIs within this window length. Then, we sequentially added either the next best performing single RI or the next most orthogonal RI (i.e., least correlated based on PCA) to the best performing RI until we tested up to four total RIs in our models. Here, the multiple RIs were input as independent predictors within the train function of the caret package to implement cross-validation, thus taking a multiple regression approach to combining RIs. Importantly, sequentially adding the next most orthogonal RI to the model ensures that the baseline AUC goes up with each RI addition, but it does not guarantee that the mean AUC from the cross validation will continually rise with each added RI (Fig 3).

Once the most accurate single or combination of RIs across all 31 diseases was identified, we computed and analyzed the lead time (Fig. 1). The lead time was calculated as the days between the start of an outbreak ($R_e \geq 1$) and the point that the RI or combination of RIs first became significant. Next, we employed a Generalized Linear Mixed Model (glmmTMB function in glmmTMB package (*39*)) with a negative binomial error distribution to test various *a prioiri* hypotheses regarding lead time highlighted in the main text. We tested the main effects of temperature, precipitation, HDI, pathogen incubation time, human population density, time series length, two pathogen traits (vector-borne or not; virus vs. bacteria), outbreak type (first outbreak in a time series or not), and all pairwise interactions between the pathogen traits, temperature, precipitation, HDI and human population density (Table S1). The parasite taxa were limited to viruses and bacteria, because our dataset had no fungi and helminths and because the sample size for protozoa was too small to justify analyses (Table S4). We compared the effects of first versus later outbreaks within time series to account for potential differences in lead time between initial and subsequent outbreaks. See the main text for the *a prioiri* hypotheses used to justify the interactions in this model. Additionally, we fitted the temperature and precipitation as quadratic polynomial

445 functions, because most organisms have an optimal temperature and moisture (*16*),
446 and treated disease types nested within regions as random intercepts. Additionally, HDI
447 was classified into low (<0.55), medium (0.55–0.699), and high (⩾0.7) categories,
448 following the recommendation of The United Nations Development Programme (*40*).
449 Figures were generated from the statistical model using the ggpredict function in the
450 ggeffects package (*41*).
451 **Time-to-event analyses.** To complement the indirect approach used by traditional RI
452 analyses, we employed a mixed effects Cox proportional hazards time-to-event analysis
453 (coxme function in coxme package (*42*)) to more directly test predictions of the timing of
454 outbreak occurrence. We used the same model structure as described for the lead time
455 analyses (Table S1). In these analyses, the response variable was a time series of 0
456 values indicating non-outbreak days ($R_e < 1$) and a single 1 value indicating the
457 outbreak point where the outbreak began ($R_e \geq 1$). Given that there is no reliable way to
458 graph the time-to-event analyses incorporating random intercepts (*43–45*), we replicated
459 the final Cox proportional hazards model in the glmmTMB package with negative
460 binomial errors, verified that the direction of the effects and significance matched
461 between the two models (final results see Table S2, S3), and then generated figures from
462 the glmmTMB model (*39*) using the ggpredict function in the ggeffects package (*41*).
463 To directly estimate lead time rather than relying on indirect estimation as done
464 by traditional RIs, we employed the parametric survival regression model (*survreg*
465 function in survival Package) (*46*), i.e., a time to an event model. In the model, the
466 predictor was the tau value (τ) of the best RIs (Standard Deviation), window length=10
467 days; Fig 3a-b). The response variable was a time series of 0 values indicating non-
468 outbreak days ($R_e < 1$) and a single 1 value indicating the hypothetical time point at
469 which the outbreak could be anticipated in advance. The lead time was computed as
470 the days between the first instance that survival regression model was significant and
471 the start of the outbreak. All analyses were conducted by R version 4.1.2 (*47*).
472
473 **Acknowledgements**
474 We thank Prof. Stephen Carpenter for feedback on this manuscript. We thank the
475 members of Rohr Laboratory of Ecology and Public Health at University of Notre Dame
476 for discussion. **Funding**: This research was supported by grants from the National
477 Science Foundation (DEB-2017785, DEB-2109293, BCS- 2307944, ITE- 2333795), US
478 Department of Agriculture (2021-38420-34065), the Frontier Research Foundation, and

the University of Notre Dame Poverty Initiative to JRR, and a grant from the University of Notre Dame Lucy Family Institute for Data and Society to JRR and NM. **Author Contributions:** J.R.R. and Q.H.Z conceptualized the study. J.R.R. supervised the study. E.N.N and M.R. supported EWS analysis. N.M. helped with the selection of the RIs. Q.H.Z. performed the study and analyzed the data. J.R.R. and Q.H.Z. wrote the original draft. All the authors reviewed and edited the manuscript. **Competing interests:** The authors declare no competing interests. **Data and materials availability:** All raw daily disease data used in this study are publicly available at ADIO (https://aido.bsvgateway.org/). All data, code, and materials used in the analysis are available on GitHub (https://github.com/QZhao16/EWs).

References

1. J. M. Drake, T. S. Brett, S. Chen, B. I. Epureanu, M. J. Ferrari, É. Marty, P. B. Miller, E. B. O'Dea, S. M. O'Regan, A. W. Park, P. Rohani, The statistics of epidemic transitions. *PLOS Computational Biology* **15**, e1006917 (2019).

2. C. Delecroix, E. H. van Nes, I. A. van de Leemput, R. Rotbarth, M. Scheffer, Q. ten Bosch, The potential of resilience indicators to anticipate infectious disease outbreaks, a systematic review and guide. *PLOS Glob Public Health* **3**, e0002253 (2023).

3. L. F. Chaves, M. Pascual, Comparing Models for Early Warning Systems of Neglected Tropical Diseases. *PLOS Neglected Tropical Diseases* **1**, e33 (2007).

4. N. C. Grassly, A. G. Shaw, M. Owusu, Global wastewater surveillance for pathogens with pandemic potential: opportunities and challenges. *The Lancet Microbe* **6** (2025).

5. M. Scheffer, *Critical Transitions in Nature and Society* (Princeton University Press, 2009; https://www.jstor.org/stable/j.ctv173f1g1).

6. M. Scheffer, J. Bascompte, W. A. Brock, V. Brovkin, S. R. Carpenter, V. Dakos, H. Held, E. H. van Nes, M. Rietkerk, G. Sugihara, Early-warning signals for critical transitions. *Nature* **461**, 53–59 (2009).

7. M. Scheffer, S. R. Carpenter, T. M. Lenton, J. Bascompte, W. Brock, V. Dakos, J. van de Koppel, I. A. van de Leemput, S. A. Levin, E. H. van Nes, M. Pascual, J. Vandermeer, Anticipating Critical Transitions. *Science* **338**, 344–348 (2012).

8. T. S. Brett, J. M. Drake, P. Rohani, Anticipating the emergence of infectious diseases. *Journal of The Royal Society Interface* **14**, 20170115 (2017).

9. C. J. Dibble, E. B. O'Dea, A. W. Park, J. M. Drake, Waiting time to infectious disease emergence. *Journal of The Royal Society Interface* **13**, 20160540 (2016).

10. M. J. Harris, S. I. Hay, J. M. Drake, Early warning signals of malaria resurgence in Kericho, Kenya. *Biology Letters* **16**, 20190713 (2020).

11. T. S. Brett, P. Rohani, Dynamical footprints enable detection of disease emergence. *PLOS Biology* **18**, e3000697 (2020).

12. T. S. Brett, E. B. O'Dea, É. Marty, P. B. Miller, A. W. Park, J. M. Drake, P. Rohani, Anticipating epidemic transitions with imperfect data. *PLoS Comput Biol* **14**, e1006204 (2018).

13. S. M. O'Regan, J. M. Drake, Theory of early warning signals of disease emergence and leading indicators of elimination. *Theor Ecol* **6**, 333–357 (2013).

14. D. A. O'Brien, C. F. Clements, Early warning signal reliability varies with COVID-19 waves. *Biology Letters* **17**, 20210487 (2021).

15. V. Dakos, E. H. van Nes, P. D'Odorico, M. Scheffer, Robustness of variance and autocorrelation as indicators of critical slowing down. *Ecology* **93**, 264–271 (2012).

16. E. A. Mordecai, J. M. Caldwell, M. K. Grossman, C. A. Lippi, L. R. Johnson, M. Neira, J. R. Rohr, S. J. Ryan, V. Savage, M. S. Shocket, R. Sippy, A. M. Stewart Ibarra, M. B. Thomas, O. Villena, Thermal biology of mosquito-borne disease. *Ecology Letters* **22**, 1690–1708 (2019).

525 17. P. H. Thrall, J. Antonovics, D. W. Hall, Host and Pathogen Coexistence in Sexually Transmitted and Vector-
526 Borne Diseases Characterized by Frequency-Dependent Disease Transmission. *The American Naturalist* **142**,
527 543–552 (1993).

528 18. M. Kummu, M. Taka, J. H. A. Guillaume, Gridded global datasets for Gross Domestic Product and Human
529 Development Index over 1990–2015. *Sci Data* **5**, 180004 (2018).

530 19. S. W. Lindsay, M. Jawara, K. Paine, M. Pinder, G. E. L. Walraven, P. M. Emerson, Changes in house design
531 reduce exposure to malaria mosquitoes. *Tropical Medicine & International Health* **8**, 512–517 (2003).

532 20. A. L. Wilson, O. Courtenay, L. A. Kelly-Hope, T. W. Scott, W. Takken, S. J. Torr, S. W. Lindsay, The importance of
533 vector control for the control and elimination of vector-borne diseases. *PLOS Neglected Tropical Diseases* **14**,
534 e0007831 (2020).

535 21. D. A. Ratkowsky, J. Olley, T. A. McMeekin, A. Ball, Relationship between temperature and growth rate of
536 bacterial cultures. *J Bacteriol* **149**, 1–5 (1982).

537 22. N. Manchal, M. K. Young, M. E. Castellanos, P. Leggat, O. Adegboye, A systematic review and meta-analysis of
538 ambient temperature and precipitation with infections from five food-borne bacterial pathogens.
539 *Epidemiology & Infection* **152**, e98 (2024).

540 23. J. M. Caldwell, A. D. LaBeaud, E. F. Lambin, A. M. Stewart-Ibarra, B. A. Ndenga, F. M. Mutuku, A. R. Krystosik,
541 E. B. Ayala, A. Anyamba, M. J. Borbor-Cordova, R. Damoah, E. N. Grossi-Soyster, F. H. Heras, H. N. Ngugi, S. J.
542 Ryan, M. M. Shah, R. Sippy, E. A. Mordecai, Climate predicts geographic and temporal variation in mosquito-
543 borne disease dynamics on two continents. *Nat Commun* **12**, 1233 (2021).

544 24. A. N. M. Kraay, O. Man, M. C. Levy, K. Levy, E. Ionides, J. N. S. Eisenberg, Understanding the Impact of Rainfall
545 on Diarrhea: Testing the Concentration-Dilution Hypothesis Using a Systematic Review and Meta-Analysis.
546 *Environ Health Perspect* **128**, 126001 (2020).

547 25. K. Levy, A. P. Woster, R. S. Goldstein, E. J. Carlton, Untangling the impacts of climate change on waterborne
548 diseases: A systematic review of relationships between diarrheal diseases and temperature, rainfall, flooding,
549 and drought. *Environ Sci Technol* **50**, 4905–4922 (2016).

550 26. Y. Dai, J. Wang, Identifying the outbreak signal of COVID-19 before the response of the traditional disease
551 monitoring system. *PLOS Neglected Tropical Diseases* **14**, e0008758 (2020).

552 27. E. L. Aiken, S. F. McGough, M. S. Majumder, G. Wachtel, A. T. Nguyen, C. Viboud, M. Santillana, Real-time
553 estimation of disease activity in emerging outbreaks using internet search information. *PLOS Computational*
554 *Biology* **16**, e1008117 (2020).

555 28. H. Zheng, W. H. Woodall, A. L. Carlson, S. DeLisle, Can long-term historical data from electronic medical
556 records improve surveillance for epidemics of acute respiratory infections? A systematic evaluation. *PLOS ONE*
557 **13**, e0191324 (2018).

558 29. S. de Lusignan, J. L. Bernal, M. Zambon, O. Akinyemi, G. Amirthalingam, N. Andrews, R. Borrow, R. Byford, A.
559 Charlett, G. Dabrera, J. Ellis, A. J. Elliot, M. Feher, F. Ferreira, E. Krajenbrink, J. Leach, E. Linley, H. Liyanage, C.
560 Okusi, M. Ramsay, G. Smith, J. Sherlock, N. Thomas, M. Tripathy, J. Williams, G. Howsam, M. Joy, R. Hobbs,
561 Emergence of a Novel Coronavirus (COVID-19): Protocol for Extending Surveillance Used by the Royal College
562 of General Practitioners Research and Surveillance Centre and Public Health England. *JMIR Public Health and*
563 *Surveillance* **6**, e18606 (2020).

564 30. M. U. G. Kraemer, J. L.-H. Tsui, S. Y. Chang, S. Lytras, M. P. Khurana, S. Vanderslott, S. Bajaj, N. Scheidwasser, J.
565 L. Curran-Sebastian, E. Semenova, M. Zhang, H. J. T. Unwin, O. J. Watson, C. Mills, A. Dasgupta, L. Ferretti, S. V.
566 Scarpino, E. Koua, O. Morgan, H. Tegally, U. Paquet, L. Moutsianas, C. Fraser, N. M. Ferguson, E. J. Topol, D. A.

Duchêne, T. Stadler, P. Kingori, M. J. Parker, F. Dominici, N. Shadbolt, M. A. Suchard, O. Ratmann, S. Flaxman, E. C. Holmes, M. Gomez-Rodriguez, B. Schölkopf, C. A. Donnelly, O. G. Pybus, S. Cauchemez, S. Bhatt, Artificial intelligence for modelling infectious disease epidemics. *Nature* **638**, 623–635 (2025).

31. Global Historical Climatology Network - Daily (GHCN-Daily), Version 3, NOAA National Centers for Environmental Information (2012); https://doi.org/10.7289/V5D21VHZ.

32. Center for International Earth Science Information NetworkCIESIN-Columbia University. (2018) Gridded Population of the World, Version 4 (GPWv4): Population Count, Revision 11. (NASA Socioeconomic Data and Applications Center). https://sedac.ciesin.columbia.edu/data/collection/gpw-v4.

33. A. Cori, N. M. Ferguson, C. Fraser, S. Cauchemez, A new framework and software to estimate time-varying reproduction numbers during epidemics. *Am J Epidemiol* **178**, 1505–1512 (2013).

34. K. M. Gostic, L. McGough, E. B. Baskerville, S. Abbott, K. Joshi, C. Tedijanto, R. Kahn, R. Niehus, J. A. Hay, P. M. D. Salazar, J. Hellewell, S. Meakin, J. D. Munday, N. I. Bosse, K. Sherrat, R. N. Thompson, L. F. White, J. S. Huisman, J. Scire, S. Bonhoeffer, T. Stadler, J. Wallinga, S. Funk, M. Lipsitch, S. Cobey, Practical considerations for measuring the effective reproductive number, Rt. *PLOS Computational Biology* **16**, e1008409 (2020).

35. Q. Zhao, QZhao16/EWs, version https://github.com/QZhao16/EWs, https://github.com/QZhao16/EWs (2023); https://github.com/QZhao16/EWs.

36. V. Dakos, S. R. Carpenter, W. A. Brock, A. M. Ellison, V. Guttal, A. R. Ives, S. Kéfi, V. Livina, D. A. Seekell, E. H. van Nes, M. Scheffer, Methods for Detecting Early Warnings of Critical Transitions in Time Series Illustrated Using Simulated Ecological Data. *PLOS ONE* **7**, e41010 (2012).

37. W. Ebisuzaki, A Method to Estimate the Statistical Significance of a Correlation When the Data Are Serially Correlated. *Journal of Climate* **10**, 2147–2153 (1997).

38. M. Kuhn, caret: Classification and Regression Training, (2007); https://doi.org/10.32614/CRAN.package.caret.

39. M. Brooks, B. Bolker, K. Kristensen, M. Maechler, A. Magnusson, H. Skaug, A. Nielsen, C. Berg, K. Van Bentham, glmmTMB: Generalized Linear Mixed Models using Template Model Builder, (2017); https://doi.org/10.32614/CRAN.package.glmmTMB.

40. U. Nations, “Data Reader’s Guide” (United Nations); https://hdr.undp.org/reports-and-publications/2020-human-development-report/data-readers-guide.

41. D. Lüdecke, F. Aust, S. Crawley, M. S. Ben-Shachar, S. C. Anderson, ggeffects: Create Tidy Data Frames of Marginal Effects for “ggplot” from Model Outputs, version 2.2.0 (2025); https://cran.r-project.org/web/packages/ggeffects/index.html.

42. T. M. Therneau, coxme: Mixed Effects Cox Models, (2009); https://doi.org/10.32614/CRAN.package.coxme.

43. R. G. Medina, R. J. Paxton, E. De Luna, F. A. Fleites-Ayil, L. A. Medina Medina, J. J. G. Quezada-Euán, Developmental stability, age at onset of foraging and longevity of Africanized honey bees (Apis mellifera L.) under heat stress (Hymenoptera: Apidae). *Journal of Thermal Biology* **74**, 214–225 (2018).

44. D. F. Moore, “book: Multiple Survival Outcomes and Competing Risks” in *Applied Survival Analysis Using R*, D. F. Moore, Ed. (Springer International Publishing, Cham, 2016; https://doi.org/10.1007/978-3-319-31245-3_9), pp. 113–135.

45. D. P. McMahon, M. E. Natsopoulou, V. Doublet, M. Fürst, S. Weging, M. J. F. Brown, A. Gogol-Döring, R. J. Paxton, Elevated virulence of an emerging viral genotype as a driver of honeybee loss. *Proceedings of the Royal Society B: Biological Sciences* **283**, 20160811 (2016).

46. T. M. Therneau, survival: Survival Analysis, (2001); https://doi.org/10.32614/CRAN.package.survival.

47. R Core Team. R: The R Project for Statistical Computing. http://R-project.org/. (2021).

48. A. Cori, N. M. Ferguson, C. Fraser, S. Cauchemez, EpiEstim: Estimate Time Varying Reproduction Numbers from Epidemic Curves, (2022); https://doi.org/10.32614/CRAN.package.EpiEstim.

49. J. Wallinga, P. Teunis, Different Epidemic Curves for Severe Acute Respiratory Syndrome Reveal Similar Impacts of Control Measures. *Am J Epidemiol* **160**, 509–516 (2004).

50. L. M. A. Bettencourt, R. M. Ribeiro, Real Time Bayesian Estimation of the Epidemic Potential of Emerging Infectious Diseases. *PLOS ONE* **3**, e2185 (2008).

51. E. Southall, T. S. Brett, M. J. Tildesley, L. Dyson, Early warning signals of infectious disease transitions: a review. *Journal of The Royal Society Interface* **18**, 20210555 (2021).

52. P. B. Miller, E. B. O'Dea, P. Rohani, J. M. Drake, Forecasting infectious disease emergence subject to seasonal forcing. *Theoretical Biology and Medical Modelling* **14**, 17 (2017).

53. I. Pavithran, R. I. Sujith, Effect of rate of change of parameter on early warning signals for critical transitions. *Chaos: An Interdisciplinary Journal of Nonlinear Science* **31**, 013116 (2021).

54. V. Dakos, C. A. Boulton, J. E. Buxton, J. F. Abrams, B. Arellano-Nava, D. I. Armstrong McKay, S. Bathiany, L. Blaschke, N. Boers, D. Dylewsky, C. López-Martínez, I. Parry, P. Ritchie, B. van der Bolt, L. van der Laan, E. Weinans, S. Kéfi, Tipping point detection and early warnings in climate, ecological, and human systems. *Earth System Dynamics* **15**, 1117–1135 (2024).

55. V. Cerqueira, N. Moniz, C. Soares, VEST: automatic feature engineering for forecasting. *Mach Learn* **113**, 4523–4545 (2024).

56. X. Wang, K. Smith, R. Hyndman, Characteristic-Based Clustering for Time Series Data. *Data Min Knowl Disc* **13**, 335–364 (2006).

57. F. Grziwotz, C.-W. Chang, V. Dakos, E. H. van Nes, M. Schwarzländer, O. Kamps, M. Heßler, I. T. Tokuda, A. Telschow, C. Hsieh, Anticipating the occurrence and type of critical transitions. *Science Advances* **9**, eabq4558 (2023).

58. E. R. Deyle, R. M. May, S. B. Munch, G. Sugihara, Tracking and forecasting ecosystem interactions in real time. *Proceedings of the Royal Society B: Biological Sciences* **283**, 20152258 (2016).

59. M. Ushio, C.-H. Hsieh, R. Masuda, E. R. Deyle, H. Ye, C.-W. Chang, G. Sugihara, M. Kondoh, Fluctuating interaction network and time-varying stability of a natural fish community. *Nature* **554**, 360–363 (2018).

60. M. Scheffer, S. R. Carpenter, T. M. Lenton, J. Bascompte, W. Brock, V. Dakos, J. van de Koppel, I. A. van de Leemput, S. A. Levin, E. H. van Nes, M. Pascual, J. Vandermeer, Anticipating Critical Transitions. *Science* **338**, 344–348 (2012).

61. M. Scheffer, S. Carpenter, J. A. Foley, C. Folke, B. Walker, Catastrophic shifts in ecosystems. *Nature* **413**, 591–596 (2001).

62. M. Scheffer, J. Bascompte, W. A. Brock, V. Brovkin, S. R. Carpenter, V. Dakos, H. Held, E. H. van Nes, M. Rietkerk, G. Sugihara, Early-warning signals for critical transitions. *Nature* **461**, 53–59 (2009).

63. V. Cerqueira, N. Moniz, C. Soares, VEST: automatic feature engineering for forecasting. *Mach Learn*, doi: 10.1007/s10994-021-05959-y (2021).

64. Y. Mei, W. He, X. Xie, S. Wan, B. Gu, Increasing Long-Term Memory as an Early Warning Signal for a Critical Transition. *Journal of Climate* **37**, 487–504 (2023).

Supplementary materials

Supplementary Figures

Figure S1. Across all 31 diseases, RIs accuracy (mean AUC from 100 runs of 5-fold cross validation) varies as a function of window lengths of 7 to 21 days. A higher AUC value (area under the curve) indicates a higher ability of a binary classifier to properly classify true positive and negative outcomes, thus representing higher accuracy for RIs. The red line represents the fit from a generalized additive model (gam function from mgcv package of R). The blue line represents a linear or quadratic fit from a linear regression model (lm function from the base package of R). The solid lines indicate significant associations, whereas dashed lines indicate non-significant associations.

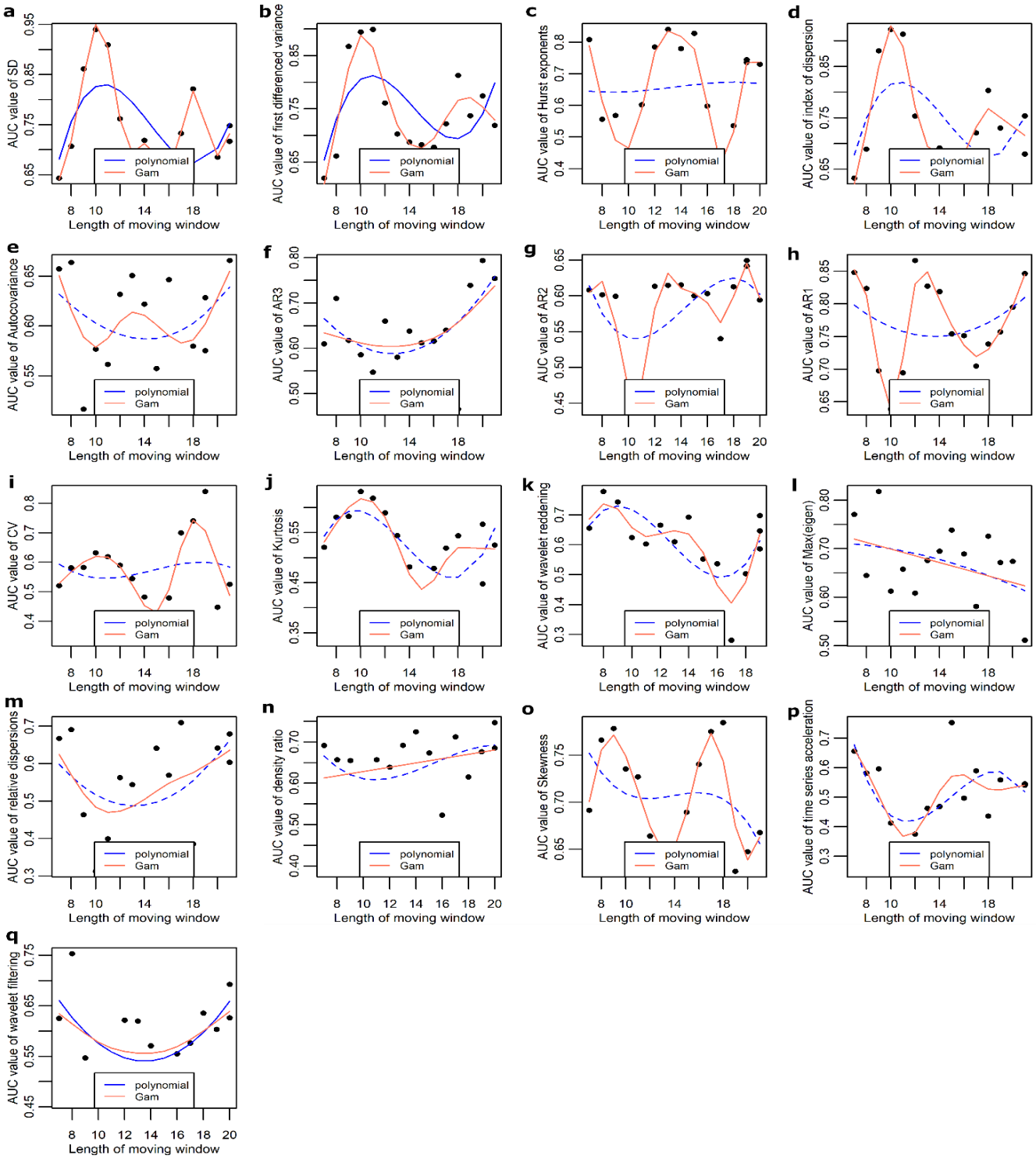

660 **Figure S2. Across all 31 diseases, the accuracy (the AUC from 100 runs of 5-fold**
661 **cross validation) of mean incidence varies as a function of window lengths of 7 to**
662 **21 days**. All methods for calculating the area under the curve (AUC) for the mean
663 incidence indicator are identical to those used for the 17 resilience indicators (see
664 Methods and Fig S1). A higher AUC value (area under the curve) indicates a higher
665 ability of a binary classifier to properly classify true positive and negative outcomes,
666 thus representing higher accuracy for RIs. The red line represents the fit from a
667 generalized additive model (gam function from mgcv package of R). The blue line
668 represents a linear or quadratic fit from a linear regression model (lm function from the
669 base package of R). The solid lines indicate significant associations, whereas dashed
670 lines indicate non-significant associations.

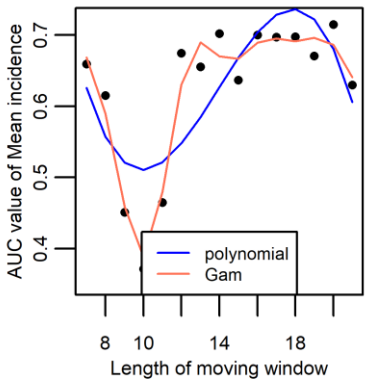

671
672

Figure S3. Coefficients ± s.e (a) and plots of tau value (τ) (b) from a Cox proportional hazards mixed model examining the effects of tau value (τ) from the best of RIs (Standard Deviation) on time to outbreak occurrence. In the model, we treated regions nested within disease types as random intercepts. The predictor was the tau value (τ). The response variable was a time series of 0 values indicating non-outbreak days ($R_e < 1$) and a single 1 value indicating the outbreak point where the outbreak began ($R_e \geq 1$). **a**, A positive coefficient signifies an increased hazard of outbreak occurrence, and consequently a reduced time until an outbreak at (b). **b**, the bold lines and gray bands depict best-fit lines and 95% confidence intervals, respectively. Significant effects are indicated by *P <0.05, **P < 0.01, ***P < 0.001.

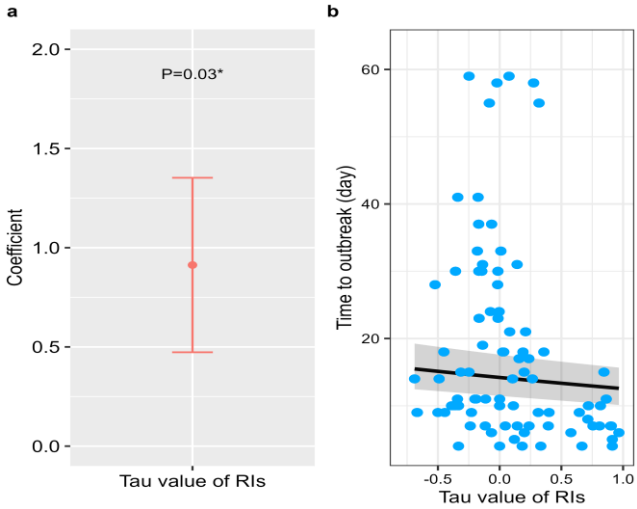

Figure S4. The lead time estimated from the time-to-event analysis based on daily data. The gray bar represents the mean, while the associated error bar illustrates the standard error. The lead time, i.e. days between the first instance that survival regression model was significant and the start of the outbreak, was computed by the best single RI (Standard Deviation, window length=10 days; Fig 3a-b, Fig S1). The predictor was the tau value (τ) of the RIs. The response variable was a time series of 0 values indicating non-outbreak days ($R_e < 1$) and a single 1 value indicating the hypothetical time point at which the outbreak could be anticipated in advance.

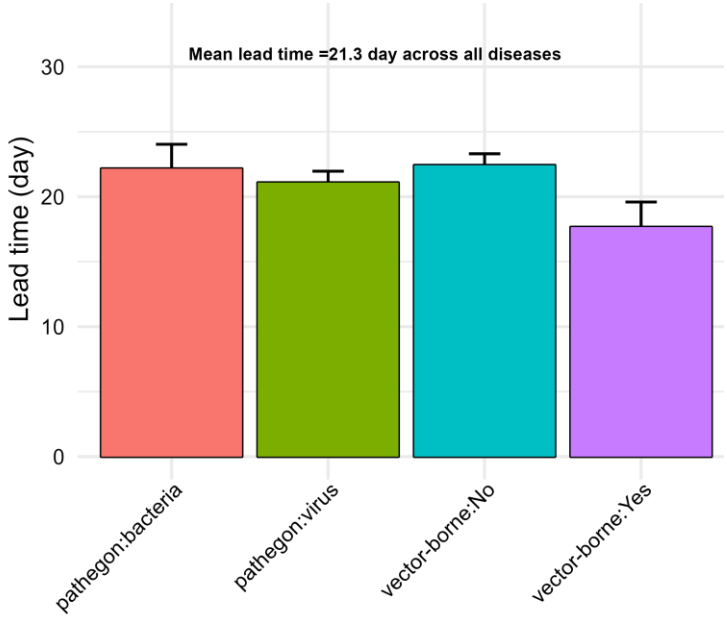

Figure S5. For the aggregated weekly data, the accuracy of resilience indicators (RIs) as early warning signals (EWSs) of outbreaks across 31 diseases, examined using mean area under the receiver operating characteristic curves (AUC) and cross validation. All RIs used the window length (i.e. 4 weeks) that maximized the AUC for the most accurate RI (i.e. Density ratio; mean AUC=0.85) (**a-b**) across all RIs and window lengths. We sequentially added either the next best performing single RI (**a**) or the next most orthogonal RI (i.e., least correlated based on Principal Component Analysis) to the best performing RI (**b**) until we tested up to four total RIs in our models. Importantly, sequentially adding the next most orthogonal RI to the model ensures that the baseline AUC goes up with each RI addition, but it does not guarantee that the mean AUC from the cross validation will continually rise with each added RI. Density ratio: DR, index of dispersion: ID, time series acceleration: TSA, standard deviation: SD, Relative dispersion: RD, Hurst exponent: HP. The AUC values in parenthesis (**a-b**) represent the mean and s.d from cross-validation.

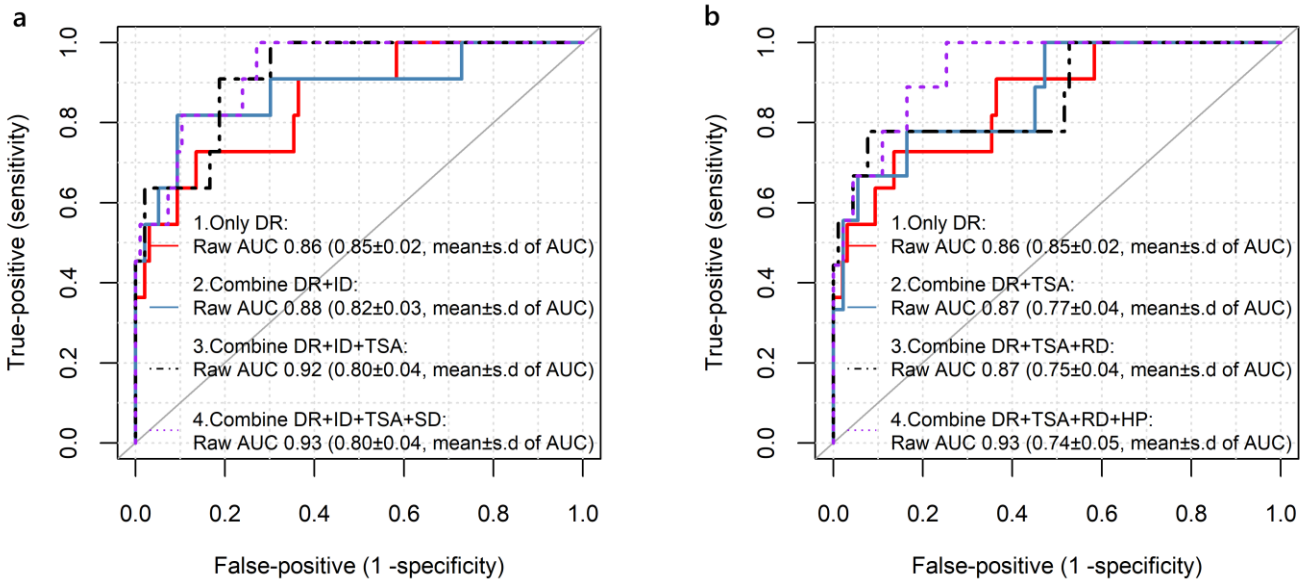

Figure S6. The lead time estimated from RIs approach based on daily and coarse-scale weekly data. The weekly data was derived by aggregating daily data to a weekly scale through weekly averaging. Apart from differences in data resolution, all other methods for calculating lead time for weekly data are identical to those applied to daily data using the RIs approach (see Methods). The gray bar represents the average, while the associated error bar illustrates the standard error. The lead time for weekly data was computed by the best performing single RI (Density ratio, window length=4 weeks; Fig. S5). For the daily data, the lead time was computed by the best performing single RI (Standard Deviation, window length=10 days; Fig3 & Fig S1).

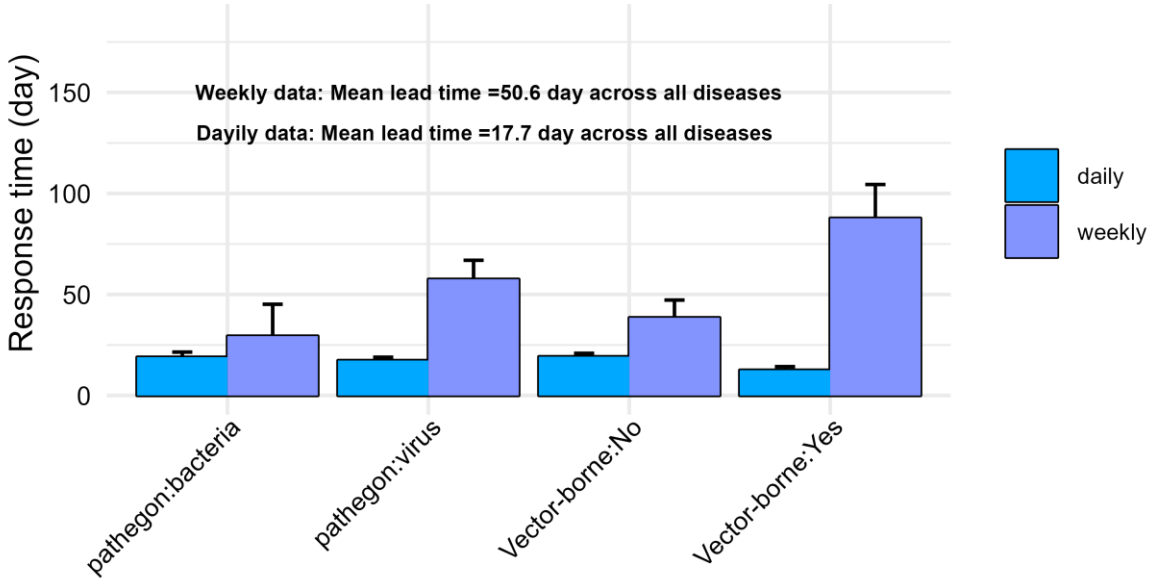

Figure S7. Effects of time series length on (a) lead time and (b) time to outbreak occurrence. Statistical results are presented in Table S1 and S3. The bold lines represent the significant best-fit trendlines, while the gray bands denote the corresponding 95% confidence bands. For the effects of the remaining variables on these response variables, refer to Figure 4 and 5.

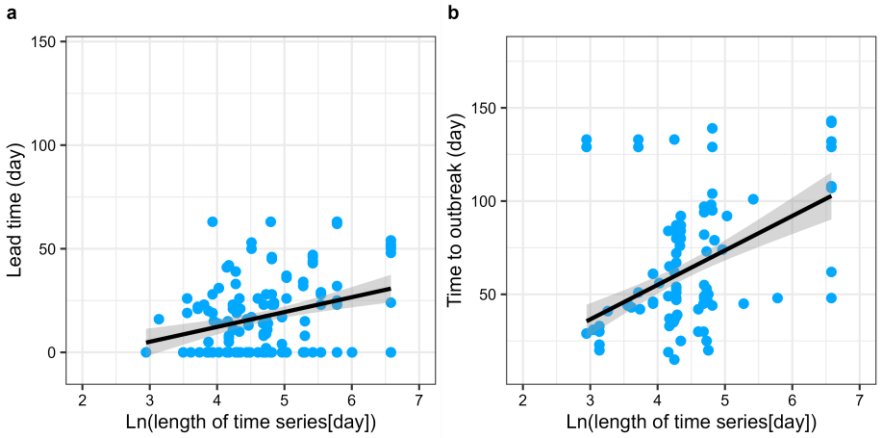

732 **Figure S8. The lead time in responses to outbreak type**. The lead time (mean ±s.e.)
733 between the first outbreaks and subsequent outbreaks in a time series had no
734 difference. Statistical results can be found in Table S1.

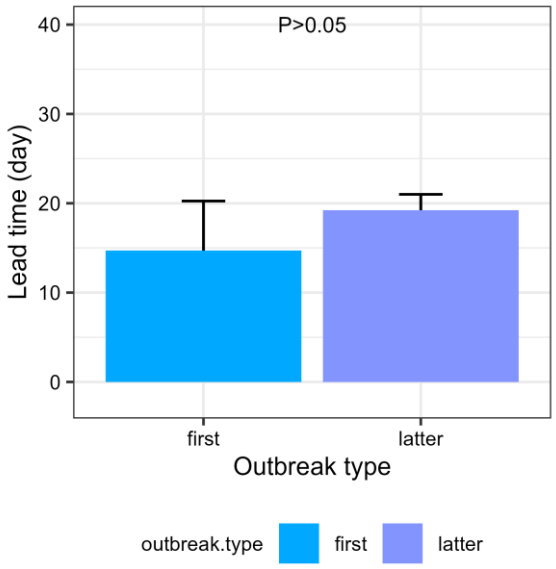

735
736

Figure S9. Effects of human population density (a, b) on the amount of lead time before disease outbreaks across 31 diseases. Dashed lines indicate non-significant trendlines. Details of statistical results are available in Table S1. For the effects of the remaining variables—temperature, precipitation, HDI, pathogen incubation time, and two parasite-pathogen traits—on lead time, refer to Figure 4.

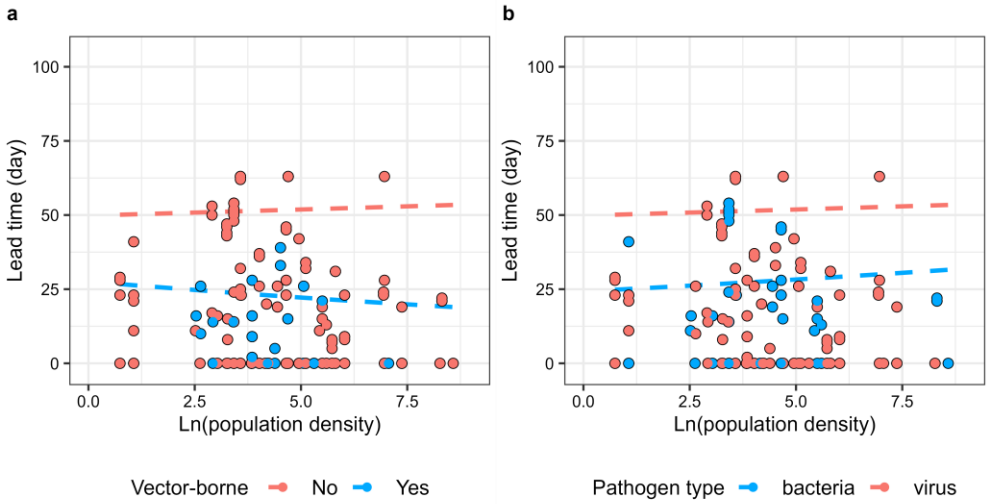

Figure S10. Frequency of the number of outbreaks per time series with the average number of secondary infections caused by a single infected individual at a given time point ($R_e \geq 1$).

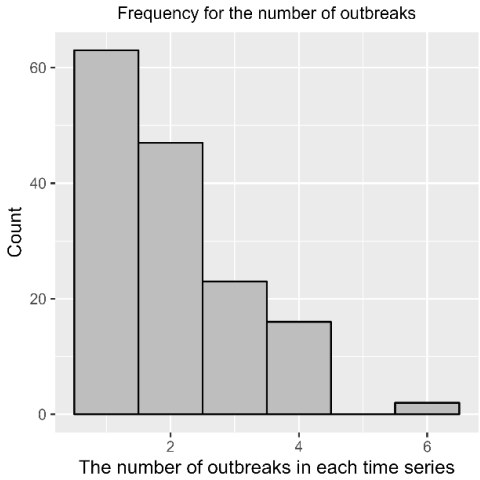

750

751 **Supplementary Information 1**

752 The method developed by Cori et al. (*33*) defined the R_e as the ratio of the number
753 of new infections at time t (I_t) to the total infectiousness of individuals up to that point.

754 $$R_e = \frac{I_t}{\sum_{s=1}^{t} I_{t-s} w_s}$$

755 The total infectiousness is expressed as $\sum_{s=1}^{t} I_{t-s} w_s$, representing the sum of infection
756 incidences from previous time steps (up to t-1), weighted by w_s. The w_s is a probability
757 distribution (hence summing to 1) describing the average infectiousness profile after
758 infection, which can be directly estimated using Markov Chain Monte Carlo
759 (dic.fit.mcmc function in coarseDataTools package) (*48*). To account for the uncertainty
760 in the distribution of w_s, we assume that w_s follows a Gamma distribution, with its
761 mean (μ) and standard deviation (σ) varying according to truncated normal distributions
762 (*33*). Following the methodology of Cori et al. (*33*), we generate 1,000 pairs of mean and
763 standard deviation, denoted as $(\sigma, \mu)^1, \ldots., (\sigma, \mu)^{1000}$, with the constraint that $\sigma < \mu$ in
764 each pair. This constraint ensures that the Gamma probability density function of w_s is
765 null at t=0. For each pair $(\sigma, \mu)^k$, we draw 1,000 realizations of R_e from its posterior
766 distribution, conditional on the corresponding $(\sigma, \mu)^k$. This process yields a total sample
767 size of 1,000,000 (1,000 × 1,000) from the joint posterior distribution of R_e. The
768 posterior mean, standard deviation, and the 0.025, 0.05, 0.25, 0.5, 0.75, 0.95, and
769 0.975 quantiles of R_e are eventually obtained from this sample.

770 Unlike methods that require fitting mechanistic dynamic models to incidence or
771 case data for estimating the R_e, the approaches developed by Cori et al. (*33*), along with
772 the other two approaches developed by Wallinga and Teunis (*49*), and Bettencourt and
773 Ribeiro (*50*), are generic and commonly used model-free method that rely on case
774 incidence data for R_e estimation. However, among the three, the method by Cori et al.
775 (*33*) had higher accuracy and addressed the limitations present in the other two
776 approaches. First, Cori et al. (*33*) uses data from before time *t*, while Wallinga and
777 Teunis (*49*) require data from after time *t* (*33*). This reliance makes the latter approach
778 conceptually and methodologically less suitable for near real-time estimation,
779 particularly when the objective is to assess the impact of interventions or other external
780 factors on transmission dynamics at a specific point in time (*33*, *34*). Second, the
781 method proposed by Cori et al. (*33*) can accommodate any positive, discrete generation
782 interval distribution. In contrast, the approach by Bettencourt and Ribeiro (*50*)

783 implicitly assumes that the generation interval follows an exponential distribution-as it
784 is derived from a Susceptible-Infectious-Recovered (SIR) model, which restricts the
785 applicability of the latter method (*33*, *34*). Third, the method developed by Cori et al.
786 (*33*) demonstrates greater robustness when applied to data with small aggregation time
787 steps (e.g., daily data), enabling the generation of smoother estimates (*34*).
788

Supplementary Information 2

Details of the 17 resilience indicators

1. *Standard deviation, Coefficient of Variation, Index of Dispersion and First differenced variance.*

As a system approaches a critical transition, the slowing rate of return to equilibrium can result in greater fluctuations facing disturbances (*36*). Large disturbances can push the system beyond the boundaries of alternative stable states—a phenomenon known as flickering. Both critical slowing down and flickering contribute to an increase in variance prior to a full transition, making it a key indicator of early warning (*36*).

Variance can be measured using standard deviation SD ($SD = \frac{1}{n}\sum_{t=1}^{n}(X_t - u)^2$) (*36*), the coefficient of variation CV ($CV = \frac{SD}{u}$) (*36*), index of dispersion ID (*36*), or first differenced variance (FDV) (*12*), The rise in variance reflects the system's diminishing ability to recover from perturbations, serving as a useful diagnostic for detecting impending state shifts.

$$FDV = \frac{1}{n-1}\sum_{t=1}^{n}(\Delta X_t - \Delta\bar{X})^2$$

Where ΔX_t is the difference among disease cases at time t and $t-1$, e.g. $\Delta X_t = X_t - X_{t-1}$. $\Delta\bar{X}$ is the mean of these difference.

2. *Skewness, Kurtosis and Density Ratio.*

Certain types of disturbances can drive the system state toward the boundary between two alternative stable states (*36*). At these boundaries, the system dynamics slow down, leading to an increased skewness (SK) of a time series, i.e. an asymmetric in distribution of observed values (*36*). Skewness is defined as the standardized third moment around the mean, capturing the degree of asymmetry in a distribution ($SK = \frac{\frac{1}{n}\sum_{t=1}^{n}(X_t-u)^3}{\sqrt{\frac{1}{n}\sum_{t=1}^{n}(X_t-u)^2}}$) (*36*).

In addition, disturbances and flickering can push the system state toward more extreme values as it approaches a critical transition (*36*). These effects lead to an increased frequency of rare events, resulting in fatter tails in the time series distribution. Consequently, the kurtosis (KU) of the time series can rise prior to the transition, reflecting an elevated occurrence of extreme deviations from the mean. Kurtosis is defined as the standardized fourth moment around the mean, capturing the heaviness of the tails in a distribution ($KU = \frac{\frac{1}{n}\sum_{t=1}^{n}(X_t-u)^4}{\left(\sqrt{\frac{1}{n}\sum_{t=1}^{n}(X_t-u)^2}\right)^2}$)(*36*).

As a system approaches a critical transition, this also results in changes in the probability density function of the system's states over time (*36*). The Density Ratio (DR) can serve as an early warning signal by identifying shifts in the probability distribution. The DR measures these changes by comparing the probability density of recent observations ($P_{present}$) to a reference (baseline) distribution from a stable period (P_{ref}) (*36*), expressed as $DR = \frac{P_{present}}{P_{ref}}$.

3. *Autocorrelation at lag 1, 2 and 3, and Autocovariance*. As a system nears a critical transition, the rate of returns to equilibrium following a small perturbation decreases (*36*). This slow rate of return is termed as critical slowing down (*36*). As the rate of return decreases, the state of the system becomes increasingly similar between consecutive observations, where the time series exhibits an increase of autocorrelation (*36*). Therefore, autocorrelation at low lags can serve as warning signals of an impending transition (*36*).

Autocorrelation at lag 1 can be measured by a conditional least-squares method to fit an autoregressive model of order 1 (AR(1)), which is expressed as:

$$X_t = \emptyset_1 X_{t-1} + \epsilon_t$$

X_t and X_{t-1} are the disease cases at time t and t-1, respectively. ϵ_t is a Gaussian white noise error term with mean zero and constant variance. $\emptyset_1$ is the autoregressive coefficient and serves as a proxy for Autocorrelation at lag 1 (*36*). Similarly, the Autocorrelation at lag 2 and 3 can be expressed as $X_t = \emptyset_2 X_{t-2} + \epsilon_t$ and $X_t = \emptyset_3 X_{t-3} + \epsilon_t$, respectively. Here $\emptyset_2$ and $\emptyset_3$ are Autocorrelation at 2 and 3, respectively.

In addition, as a system nears a transition, the decline in the rate of return causes deviations from equilibrium for longer periods. This prolonged persistence increases the dependence between observed values in the time series, resulting in elevated autocovariance (AU)(*10, 51*). Autocovariance can thus serve as a metric for quantifying the persistence of fluctuations $AU = \frac{1}{n-1}\sum_{t=1}^{n-1}(X_t - \bar{X})(X_{t-1} - \bar{X})$ (*10, 51*).

4. *Wavelet filtering and Wavelet reddening.*

When disease transmission is subject to seasonal forcing, wavelet-based warning signals can capture the temporal variability of disease dynamics and serve as robust indicators of impending epidemiological changes (*52*).

As Miller et al (*52*), Wavelet filtered reddening WF is defined as any quantity proportional to the variance of the time series after it is filtered to include only its components in a wavelet transform's frequency domain, calculated as $WF = \frac{0.34T\delta_t}{\lambda}\sum_{j=j1}^{j2}\frac{|(W_t(S_j)|^2}{S_j}$, where T is length of the time series, δ_t is the difference in time between observations, λ represents the ratio of the Fourier period of the wavelet function to its corresponding scale, S_j is a wavelet scale and $W_t(S_j)$ represents the wavelet transform of the observed disease time series, localized at time index t and the wavelet scale S_j (*52*). All parameters within the equation for WF was estimated in accordance with the methodology of Miller et al. (*52*).

Next, wavelet spectral reddening (WR) is defined as the median scale of the wavelet spectral density at a given time t, expressed as $WR = min\{S_j \; such \; that \; \bar{w}_{t,1j}^2/\bar{w}_{t,1j_{max}}^2\}$, where the wavelet scale increases from 1 to j_{max} (*52*).

5. *Hurst exponent, Relative dispersion, and Time series acceleration.*

As a system approaches critical slowing down, the *Hurst exponent* (HE) is expected to increase, and it has been demonstrated to effectively predict the transition in advance of the tipping point (*53, 54*). HE is calculated by the algorithm of Multifractal detrended fluctuation analysis, where the HE is computed as the linear slope for the variation of fluctuations F^2 against the span size w (*53*). Here, the variation of fluctuations F^2 is determined as $F^2 = \frac{1}{w}[\sum_{t=1}^{w}(Y_i - \bar{Y}_i)^2]$, where Y_i the cumulative deviation series from the overall mean of the time series and expressed as $Y_i = \sum_{t=1}^{N}(x_i - \bar{x})$ (*53*). The $\bar{Y}_i$ is the polynomial fit of order 1 against each of these segments w. The w is to divide the entire time series into non-overlapping segments, and the w varies from 2 to $N-2$, where the N is the length of entire time series.

Following the Cerqueira et al. (*55*) and Wang et al. (*56*), *Relative Dispersion* is estimated as the ratio between the standard deviation of the time series and the standard deviation of the differenced time series. *Time series acceleration* the second derivative of the observed values with respect to time, which is expected to decrease as the system nears to tipping point (*55*).

6. *The absolute value of dominant eigenvalue (Max(eigen)).*

Theoretically, as a discreate time system nears a tipping point, the absolute value of dominant eigenvalue (Max(eigen)) from Jacobian Matrix approaches 1 (*57*). The elements in Jacobian matrix (***J***) can be estimated by S-map, $X_i(t+1) = \sum_{j=1}^{E} \boldsymbol{J}\, X_j(t) + C_0$, where E is the embedding dimension consisting of number of E state variables (*57*, *58*). The S-map algorithm constructs a local linear model (**C**) to predict the future state at time $t+1$ using the state vector X_j from the reconstructed state space (*57*, *58*). However, unlike traditional linear regression models, the linear approximation in the S-map algorithm is performed locally, assigning greater weights to data points that are in close to the target state vector X_j (*57*, *58*).

For the disease cases time series, the S-map algorithm reconstructs the Jacobian matrix (***J***) using a single observed variable (i.e., disease cases). This follows the principle of lagged coordinate embedding (i.e., univariate embedding), which reconstructs the underlying system's state space from time-delayed versions of the univariate time series (*57*). Since the reconstructed state space is a delay embedding of a univariate time series, the resulting Jacobian matrix (***J***) is characterized by a sparse structure. Specifically, all elements of ***J*** are zero except for the lower off-diagonal elements, which are equal to unity, and the first row, which contains the nontrivial linear approximation that governs the system's local dynamics (*57*).

$$\begin{pmatrix} X(t+1) \\ X(t) \\ \vdots \\ X(t-E+2) \end{pmatrix} = \begin{pmatrix} \overbrace{\begin{matrix} J_{11} & J_{12} & \cdots & J_{1E} \\ 1 & 0 & \cdots & 0 \\ 0 & \ddots & \ddots & \vdots \\ \cdots & 0 & 1 & 0 \end{matrix}}^{\text{Jacobian matrix } \boldsymbol{J}} \end{pmatrix} \begin{pmatrix} X(t) \\ \vdots \\ (t-E+2) \\ X(t-E+1) \end{pmatrix} + \begin{pmatrix} V_1 \\ 0 \\ \vdots \\ 0 \end{pmatrix}$$

Since the Jacobian matrix (***J***) is evaluated at each time point t (i.e., the local Jacobian $\boldsymbol{J}_t$), it exhibits time-varying dynamics. From these local Jacobians, the absolute value of the dominant eigenvalue *(Max(eigen))* can be computed at each time step, providing insights into the temporal changes of the disease system's stability shifting from disease free to outbreak states (*57*). The best embedding dimension E is selected by using the simplex projection that gave the lowest mean absolute error (*59*).

Supplementary tables

Table S1. Results from a generalized linear mixed model examining the main effects of temperature, precipitation, human development index (HDI), pathogen incubation time, human population density, time series length, two pathogen traits (vector-borne or not; virus vs. bacterial pathogen), outbreak type (first or subsequent outbreak in a time series), and the pairwise interactions between the two pathogen traits and temperature, precipitation, HDI and human population density on lead time. In the model, we treated regions nested within disease types as random intercepts. The parasite taxa were limited to viruses and bacteria because our dataset had no fungi or helminths (Table S4) and the sample size for protozoa was too small to justify analysis (only two parasite species). A significant quadratic coefficient indicates a second-order polynomial function between a predictor and lead time. The blue text denotes non-significant predictors that were removed from the final model through a backward sequential selection. ***P< 0.001, **P<0.01, *P<0.05. The model's marginal R^2 is 0.12, and the conditional R^2 is 0.17. The model AIC value before and after removing the blue non-significant predictors was 1131.57 and 1121.83, respectively.

Independent variable	**coefficient**	**s.e**	**Z**	**P value**
Final model				
(Intercept)	2.30	0.31	7.46	**<0.0001*** **
Temperature	4.72	1.13	4.17	**<0.0001*** **
Temperature^2	-1.18	1.36	-0.87	0.39
Precipitation	-3.00	1.21	-2.49	**0.01***
Precipitation^2	-0.05	0.78	-0.06	0.95
HDI (low)	-0.74	0.13	-5.72	**<0.0001*** **
HDI (medium)	-0.29	0.13	-2.30	**0.02***
Incubation time	0.11	0.05	2.16	**0.03***
Length time series	0.17	0.06	2.69	**0.007** **
Pathogen type	0.30	0.15	1.94	0.05
Vector borne	-2.89	0.70	-4.13	**<0.0001*** **
Temperature: Pathogen type	-2.00	1.28	-1.56	0.12
Temperature^2: Pathogen type	-4.31	1.62	-2.66	**0.007** **
Precipitation: Pathogen type	3.94	1.32	2.99	**0.002** **
Precipitation^2: Pathogen type	-2.04	0.97	-2.10	**0.03***
Temperature: Vector borne	56.40	19.27	2.93	**0.003** **
Temperature^2: Vector borne	-33.38	12.06	-2.77	**0.005** **
Precipitation: Vector borne	-7.70	2.91	-2.65	**0.008** **
Precipitation^2: Vector borne	-3.89	1.83	-2.13	**0.03***
Non-significant predictors below were removed from the final model through a backward sequential selection.				
Population density				
Population density: Vector borne				
Population density: Pathogen type				
Outbreak type				
HDI (low): Vector borne				
HDI (medium): Vector borne				

Table S2. Results from a mixed effect Cox proportional hazard model examining the main effects of temperature, precipitation, human development index (HDI), pathogen incubation time, human population density, time series length, two pathogen traits (vector-borne or not; virus vs. bacterial pathogen), outbreak type (first or subsequent outbreak in a time series) and the pairwise interactions between the two pathogen traits and temperature, precipitation, HDI and human population density on the timing of outbreak occurrence. In the model, we treated regions nested within disease types as random intercepts. The parasite taxa were limited to viruses and bacteria because our dataset had no fungi or helminths (Table S4) and the sample size for protozoa was too small to justify analysis (only two parasite species). A positive coefficient signifies an increased hazard of outbreak occurrence, and consequently a reduced time until an outbreak. A significant quadratic coefficient indicates a second-order polynomial function between a predictor and hazard of outbreak occurrence. The blue text denotes non-significant predictors that were removed from the final model through a backward sequential selection. Model's Nagelkerke R^2 is 0.29. ***P< 0.001, **P<0.01, *P<0.05. The model AIC value before and after removing the blue non-significant predictors was 536.73 and 520.35, respectively.

Independent variable	coefficient	s.e	Z	P value
Final model				
Temperature^2	7.36	1.44	5.10	**<0.0001*** **
Temperature	-1.29	1.44	-0.90	0.36
Precipitation^2	2.97	0.67	4.43	**<0.0001*** **
Precipitation	0.14	0.76	0.18	0.85
HDI (low)	0.95	2.09	0.46	0.64
HDI (medium)	0.12	2.04	0.06	0.95
Length time series	-4.21	0.83	-5.05	**<0.0001*** **
Pathogen type	5.06	1.94	2.60	**0.009** **
Vector borne	-0.45	2.42	-0.19	0.85
Temperature^2: Pathogen type	-8.01	1.56	-5.15	**<0.0001*** **
Temperature: Pathogen type	-3.20	1.70	-1.88	0.06
Precipitation: Vector borne	-5.43	1.05	-5.18	**<0.0001*** **
Precipitation^2: Vector borne	-2.30	0.93	-2.47	**0.01* **
HDI (low): Vector borne	14.60	4.09	3.57	**0.0003*** **
HDI (medium): Vector borne	12.29	3.92	3.14	**0.001** **
Non-significant predictors below were removed from the final model through a backward sequential selection.				
Population density				
Population density: Pathogen type				
Population density: Vector borne				
Incubation time				
Outbreak type				
Precipitation: Pathogen type				
Precipitation^2: Pathogen type				
Temperature^2: Vector borne				
Temperature: Vector borne				

934 **Table S3**. Given that there is currently no reliable way to visualize the results of a Cox
935 proportional hazards (coxme) model, we replicated the final coxme model (Table S2) as a
936 generalized linear mixed model (glmmTMB function in glmmTMB package) with time to
937 an outbreak as a negative binomial dependent variable, shown below. Given that the
938 statistical outcomes of the two models had verified direction (i.e. a positive coefficient in
939 Table S2 signifies an increased hazard of outbreak occurrence and consequently a
940 reduced time until an outbreak in Table S3, and vice versa) and similar significance
941 levels, we used the glmmTMB to generate figures using the ggpredict function in the
942 ggeffects R package.

Independent variable	coefficient	s.e	Z	P value
Temperature^2	-1.27	0.46	2.75	**0.006****
Temperature	3.73	0.62	6.03	0.06
Precipitation^2	-3.63	0.62	-5.85	**<0.0001*****
Precipitation	-0.26	0.63	-0.42	0.67
HDI (low)	-0.03	0.11	-0.27	0.79
HDI (medium)	-0.13	0.12	1.15	0.25
Length time series	0.21	0.04	4.77	**<0.0001*****
Pathogen type	-1.10	0.08	-1.14	**0.04***
Vector borne	0.11	0.18	-0.61	0.54
Temperature^2: Pathogen type	3.07	1.12	-2.68	**0.007****
Temperature: Pathogen type	2.32	1.05	-2.12	0.05
Precipitation: Vector borne	3.12	1.26	2.46	**0.01***
Precipitation^2: Vector borne	1.84	0.91	2.05	**0.04***
HDI (low): Vector borne	-0.73	0.22	-3.40	**0.0006*****
HDI (medium): Vector borne	-0.14	0.25	0.15	**0.03***

943

944

Table S4. All 31 diseases used in the analyses, their corresponding regions, and traits of their pathogens and time series.

	Disease	Location	Zoonotic	Vector-borne	Pathogen type	Length of time series (mean ± s.e)
1	Anthrax	California, US Muchinga, Zambia Shaanxi, China West Bengal, India	Yes	No	bacteria	80±20
2	Brucellosis	Kyustendil, Bulgaria Qatar	Yes	No	bacteria	185±15
3	Campylobacteriosis	Australia Greece Hastings, New Zealand Northumberland, UK Kentucky, US Norway Barcelona, Spain Stockholm, Sweden Las Vegas, US Adelaide, Australia Anchorage, US	Yes	No	bacteria	175±8
4	Chikungunya	Mauritius Champasak, Laos Montpellier, France Guangdong, China Kampong Speu, Cambodia Ravenna, Italy West Bengal, India Chennai, India	No	Yes	virus	86±15
5	Cholera	Vietnam Sekong, Laos Orissa, India Haiti	No	No	virus	164±10
6	Dengue	Madeira, Portugal	No	Yes	virus	176±12
7	Ebola	Kibale, Uganda Kasai-Occidental, Congo	Yes	No	virus	112±30
8	Gastroenteritis	Belgium Pisco, Peru San Vicente, El Salvador Finland	Yes	No	Multiple types	174±20
9	Lassa Fever	Jos, Nigeria	Yes	No	virus	82±0
10	Leptospirosis	Illinois, US Guyana Fiji Martinique, France Peru Malaysia Nicaragua	Yes	Yes	protozoan	86±16

949
950 **Table S4 (continued)**.

	Disease	Location	Zoonotic	Vector-borne	Pathogen type	Length of time (mean ± s.e)
11	Malaria	Sierra Leone Amhara, Ethiopia Montserrado, Liberia Aswan, Egypt Honduras	No	Yes	protozoan	70±6
12	Marburg	Uganda Kabale, Uganda	Yes	No	virus	180±24
13	Measles	California, US Vancouver, US Federated States of Micronesia Casa Grande, US Ohio, US Mayuge, Uganda Samoa Fiji Somali, Ethiopia San Diego, US New York, US	No	No	virus	118±26
14	Middle East Respiratory Syndrome (MERS-CoV)	South Korea Jordan	Yes	No	virus	176±12
15	Monkeypox	Équateur, Congo US Impfondo, Congo Liberia Congo	Yes	No	virus	142±28
16	Nipah	Bangladesh Philippines	Yes	No	virus	189±40
17	Novel Influenza A	Australia Mexico Kyrgyzstan Jalisco, Mexico Peru Gelderland, Netherlands Hong Kong Turkey Shanghai, China Manitoba, Canada	Yes	No	virus	106±30
18	Pertussis	Spain	No	No	bacteria	166±0
19	Plague	Maharashtra, India Madagascar Eastern, Zambia Colorado, US	Yes	Yes	bacteria	87±5

951
952

953
954 **Table S4 (continued)**.

	Disease	Location	Zoonotic	Vector-borne	Pathogen type	Length of time (mean ± s.e)
20	Norovirus	New Zealand Washington, US Michigan, US Germany Michigan, US Alberta, Canada Beijing, China New Jersey, US France Malta Singapore Saint Thomas, United States Virgin Islands UK Israel Wisconsin, US Wuxi, China California, US Netherlands Japan Spain El Paso, US Colorado, US Ireland	No	No	virus	177±4
21	Polio	Madagascar Tajikistan	No	No	virus	159±6
22	Q Fever	Hungary Nova Scotia, Canada Slovenia Iraq UK Israel Bulgaria	Yes	Yes	bacteria	164±12
23	Rift Valley Fever	South Africa Uganda Madagascar Kenya Mayotte, France	Yes	Yes	virus	135±57
24	Rubella	Kenya Zimbabwe	No	No	virus	162±4

955
956

957 **Table S4 (continued)**.

	Disease	Location	Zoonotic	Vector-borne	Pathogen type	Length of time (mean ± s.e)
25	Salmonellosis	Germany Rhode Island, US District of Columbia, US Poitier, France South Korea UK Sousse, Tunisia Madrid, Spain	Yes	No	bacteria	173±21
26	Shiga Toxin-Producing E. Coli (STEC)	Michigan, US Germany UK Kanazawa, Ishikawa, Japan Iceland Netherlands Ireland	Yes	No	bacteria	225±30
27	Shigellosis	Kirkenes, Norway Sichuan, China North Carolina, US Morobe, Papua New Guinea Sweden Virginia, US Honolulu, US Pemagatsel, Bhutan Norway Salzburg, Austria Austria	No	No	bacteria	179±16
28	Tularemia	Germany Utah, US France	Yes	Yes	bacteria	183±12
29	West Nile Virus	Michigan, US Thessaloniki, Greece Romania Italy	Yes	Yes	virus	145±16
30	Yellow Fever	Sudan San Pedro, Paraguay São Paulo, Brazil	Yes	Yes	virus	92±16
31	Zika	San Andrés, Colombia Girardot, Colombia	No	Yes	virus	120±25

958
959

Table S5. List of 17 resilience indicators (RIs) used to detect critical transitions, and their type, abbreviation, and reference. The details of the 17 resilience indicators RIs see Supplementary information 2.

Indicators	Type	Abbreviation	References
1. Autocorrelation at lag 1	Commonly used indicators	AR1	(*60–62*)
2. Autocorrelation at lag 2		AR2	
3. Autocorrelation at lag 3		AR3	
4. standard deviation		SD	
5. Skewness		SK	
6. Kurtosis		KU	
7. Coefficient of variation		CV	
8. First differenced variance		FD	
9. Autocovariance		AU	
10. Index of dispersion		ID	
11. Density ratio		DR	
12. Wavelet filtering	Wavelet spectrum analysis to handle the seasonality	WF	(*52*)
13. Wavelet reddening		WR	
14. Relative dispersion	Automatic Feature Engineering for Forecasting	RD	(*53*, *63*, *64*)
15. Hurst exponent		HE	
16. Time series acceleration		TSA	
17.The absolute value of dominant eigenvalue (Max(eigen))	Empirical dynamic modelling	ME	(*57*)